Ribosomal ubiquitination facilitates mRNA cleavage and ribosome rescue during No-Go and Nonstop mRNA Decay

Parissa C. Monem[1], Audrey L. Piatt[1], Nitin Vidyasagar[1], Marissa L. Glover[1], Thea A. Egelhofer[1], Joshua A. Arribere[1,2,*]

[1]Department of Molecular, Cell, and Developmental Biology, University of California at Santa Cruz, Santa Cruz, CA, USA

[2]Lead Contact

*Correspondence: jarriber@ucsc.edu

ABSTRACT

During translational surveillance, ribosomes play a critical role in detecting problematic mRNAs and signaling cellular machinery to repress the offending messages. Prior work has shown that problematic mRNAs identified by two surveillance pathways (Nonstop and No-Go mRNA Decay) are detected by ribosome collisions and subsequent ribosomal ubiquitination, yet how ribosomal ubiquitination leads to repression has remained unclear. Here, we deploy *C. elegans* to unravel the series of coordinated events during Nonstop and No-Go mRNA Decay. We probe the metazoan SKI RNA helicase complex to uncover functionally significant residues and reveal divergence of the SKI-exosome interface. We define a functional requirement for ubiquitination on at least two ribosomal proteins during No-Go mRNA Decay, and illustrate how ubiquitination recruits the endonuclease NONU-1 via CUE domains and the ribosome rescue factor HBS-1 via its poorly characterized N-terminus. Our molecular characterization (1) underscores the importance of ribosomal ubiquitination in mRNA degradation, (2) shows similar and distinct genetic dependencies of factors in Nonstop and No-Go mRNA Decay, and (3) uncovers a conspicuous absence of distinct ribosomal stalls at No-Go mRNA Decay substrates. Our work demonstrates mechanisms by which translation signals to effectors of co-translational mRNA repression and has implications for the study of translation and ribosomal species *in vivo*.

INTRODUCTION

An organism's growth, function, and response to environmental changes rely on ribosomes accurately producing proteins. Subtle errors in mRNAs are often elusive, requiring active translation to detect the error and trigger downstream repression. If left unchecked, defective mRNAs have the potential to produce toxic proteins resulting in disease phenotypes, such as neurodegeneration seen in mice (Ishimura et al., 2014; Bengtson and Joazeiro, 2010). Ribosomes that translate problematic mRNAs can elicit various repressive mechanisms, thus ensuring proper gene expression. Two such mechanisms are Nonstop mRNA Decay and No-Go mRNA Decay. Nonstop mRNA Decay is triggered by mRNAs lacking stop codons, which are formed by premature polyadenylation or mRNA cleavage (Frischmeyer et al., 2002). No-Go mRNA Decay occurs on mRNAs containing a variety of elongation-inhibiting features, such as stable secondary structures, stretches of rare codons, polybasic amino acid-encoding sequences, or damaged nucleotides (Doma and Parker, 2006). While triggered by different mRNA species, both of these pathways result in mRNA decay, ribosome rescue, and nascent peptide degradation through the coordinated recruitment of several effectors.

Two modes of mRNA repression are exonucleolytic decay and endonucleolytic cleavage. Key to exonucleolytic decay is the SKI RNA helicase complex, which is required for mRNA decay in multiple translational surveillance pathways (Frischmeyer et al., 2002; Doma and Parker, 2006; Arribere and Fire, 2018). Two non-mutually exclusive models for SKI function exist: one points to a role in loading the 3'>5' exosome to degrade offending mRNAs (Araki et al., 2001; van Hoof et al., 2002; Doma and Parker, 2006; Hashimoto et al., 2017; Kowalinski et al., 2016), while another places the SKI complex acting alone by extracting RNA from ribosomes (Zinoviev et al., 2020). Which of these functions is essential to SKI-mediated repression remains unclear. Endonucleolytic cleavage can initiate mRNA repression through downstream decay by cellular exonucleases. Recently identified in both *C. elegans* and *S. cerevisiae,* NONU-1/Cue2/YPL199C are endonucleases responsible for cleaving targets of Nonstop and No-Go mRNA Decay in the vicinity of stalled ribosomes (Glover et al., 2020; D'Orazio et al., 2019). While NONU-1 is required for efficient Nonstop and No-Go mRNA Decay, it remains unclear how and when the factor is targeted to stall-inducing mRNAs. However, clues to its recruitment mechanism exist: NONU-1 and its homologs contain at least two conserved ubiquitin-binding domains.

During both Nonstop and No-Go mRNA Decay, ribosomes on problematic mRNAs are rescued and their nascent peptides are degraded. HBS-1 is a GTPase homologous to eRF3 and is thought to function in ribosome rescue by loading PELO-1/Dom34 (homologous to eRF1) in a codon-independent manner (Doma and Parker, 2006; Shoemaker et al., 2010; Becker et al., 2011; Saito et al., 2013; Hilal et al., 2016). Recruitment of PELO-1 leads to ribosome subunit-splitting by the AAA ATPase ABCE-1 and the eventual proteasomal degradation of the nascent peptide (Pisareva et al., 2011; Shao et al., 2014). While the precise recruitment mechanism of HBS-1 and PELO-1 is assumed to be via PELO-1 recognition of an empty ribosomal A-site, additional data showing HBS-1/PELO-1 acting on internally-stalled ribosomes challenges this model (Pisareva et al., 2011).

Recent advances have been made towards characterizing the early steps of No-Go mRNA Decay. One key upstream event is the generation of a stalled, collided ribosome species at a problematic site on the mRNA. This species is thought to be unique to No-Go mRNA Decay and could conceivably recruit downstream effectors (Simms et al., 2017; Juszkiewicz et al., 2018; Ikeuchi et al., 2019). The interface between collided ribosomes is the site of ubiquitination events on multiple ribosomal proteins near the mRNA's path (Juszkiewicz et al., 2018; Ikeuchi et al., 2019). The conserved E3 ubiquitin ligase ZNF-598 is thought to deposit ubiquitin marks on at least two ribosomal proteins, including RPS-10 (eS10) and RPS-20 (uS10) (Juszkiewicz & Hegde, 2017; Sundaramoorthy et al., 2017). These ubiquitin marks are thought to act as signaling mechanisms for further events.

Prior work highlights the importance of ribosomal ubiquitination in No-Go mRNA Decay, but has yet to fully understand its downstream consequences. This limitation is in part due to the difficulty in recovering viable mutants of the target ribosomal proteins, which has thus complicated a straightforward analysis of individual ubiquitination sites. Harnessing a system to study the functional contributions of ribosomal ubiquitination is likely to clarify downstream events. While structural studies revealed multiple collided ribosome structures with ubiquitination sites at the collision interface, the relationship of these collided structures to *in vivo* stalls on mRNAs remains poorly understood. Several recent studies have mapped the locations of ribosome species thought to represent collisions, known as disomes or di-ribosomes (Meydan et al., 2020; Han et al., 2020; Arpat et al., 2020; Zhao et al., 2021). However, the application of these data to No-Go mRNA Decay is lacking, in part due to the absence of work containing validated reporters and the lack of bonafide endogenous No-Go

mRNA Decay targets. Additionally, our current understanding of ribosomal ubiquitination by ZNF-598 relies on work utilizing reporters with stalls akin to No-Go mRNA Decay exclusively (Garzia et al., 2017; Juszkiewicz and Hegde, 2017; Sundaramoorthy et al., 2017). Given that Nonstop and No-Go mRNA Decay arise on distinct mRNA substrates, a more complete illustration of ribosomal ubiquitination function requires a consideration of both pathways.

Here, we deployed *C. elegans* to unravel the series of events during Nonstop and No-Go mRNA Decay. Unlike most metazoans, mutants of surveillance and decay machinery are viable in *C. elegans*, making it a genetically tractable system for this work. Through our Nonstop mRNA Decay reporter, we probed the function of the metazoan SKI complex and provided support for exosome-independent mRNA repression. We uncovered a functional role for ribosomal ubiquitination by ZNF-598 in recruiting both NONU-1 and HBS-1 to stalled ribosomes during No-Go mRNA Decay, revealing a novel and conserved Ub-binding function for the poorly characterized N-terminus of HBS-1. Additionally, we found that site-specific mutation of ribosomal ubiquitination targets RPS-10 (eS10) and RPS-20 (uS10) together phenocopy knock out of ZNF-598, and are required to elicit full No-Go mRNA Decay. Interestingly, while we observed a requirement of HBS-1/PELO-1 and NONU-1 in both Nonstop and No-Go mRNA Decay, we uncovered differential dependencies on ZNF-598, suggesting an alternative E3 ligase acts in Nonstop mRNA Decay. Our subsequent results via RNA-seq and Ribo-seq substantiated the importance of ZNF-598 in destabilizing No-Go mRNAs and shed light on the molecular dynamics of ribosomal stalling.

RESULTS

Novel Nonstop mRNA Decay suppressors identify functionally important residues in the SKI complex

To characterize the genetic requirements of Nonstop mRNA Decay, we used a Nonstop mRNA Decay reporter we previously constructed by CRISPR/Cas9 (Fig 1A) (Arribere and Fire, 2018). Briefly, the reporter encodes the muscle myosin *unc-54*, GFP, a T2A ‘stop-and-go’ peptide, and no in-frame stop codons. Strains with the *unc-54(nonstop)* construct efficiently degrade mRNAs from this locus via Nonstop mRNA Decay, conferring little movement and very low GFP fluorescence, whereas strains with a compromised Nonstop mRNA Decay pathway exhibit increased movement and GFP fluorescence. In prior work, we used the *unc-54(nonstop)* reporter to identify seventeen mutations in the Nonstop mRNA Decay machinery. Here, we

report the identification of an additional fourteen mutations, starting with twelve mutations in SKI complex subunits (Fig 1B).

Of the twelve mutations in SKI complex subunits, eight were in *skih-2* (*S. cer SKI2*) and four were in *ttc-37* (*S. cer SKI3*). The *skih-2* mutations were exclusively missense mutations and hit residues conserved from *S. cerevisiae* to humans (Fig S1). The majority of the *skih-2* suppressors were in the catalytic RecA domains of this protein, or lined the mRNA binding channel (Fig S1). Identification of these mutations is consistent with mRNA binding and catalysis by the SKIH-2 helicase as being required for Nonstop mRNA Decay, consistent with prior work across experimental systems. We expect that future work with these mutations will further our understanding of SKI function. Two mutations (G363E and G367E) were close to the interface of Ski2 and Ski8; existence of such mutations suggests that this interface and/or Ski8 may also be important in *C. elegans*, though we did not identify a single mutation in a factor that could conceivably function as Ski8 (see below). All four of the novel *ttc-37* suppressors were premature stop codons and will not be discussed further.

Our subsequent analysis of the *ttc-37* and *skih-2* genes agreed with a model where these two genes function together as a complex. We observed a similar fold de-repression in *ttc-37* and *skih-2* mutants (Fig 1C). Furthermore, we observed epistasis: a *skih-2 ttc-37* double mutant exhibited a similar fold de-repression to the single mutants (Fig 1C). These results are consistent with SKI complex function requiring the activity of both Ski2/Ski3-like subunits, in line with how this complex is thought to function in yeast and humans (Halbach et al., 2013; Kalisiak et al., 2017).

A novel ribosome stalling screen identifies core No-Go mRNA Decay machinery

To establish *C. elegans* as a system to study No-Go mRNA Decay, we built a ribosome stalling reporter using CRISPR/Cas9 (Fig 1D). As with our Nonstop mRNA Decay reporter, we started with the *unc-54* locus and C-terminally added a T2A ‘stop-and-go’ peptide, FLAG, twelve rare arginine codons, and GFP followed by a stop codon. We selected rare arginine codons for two reasons: (1) arginine is a positively charged amino acid and prior work (Lu and Deutsch, 2008; Chandrasekaran et al., 2019) suggests this may induce ribosome stalling via interactions with the peptide exit tunnel, and (2) the Arg-tRNAs decoding two of the rarest codons (CGG, AGG) in *C. elegans* are very lowly expressed under normal growth conditions (Aidan Manning, Todd Lowe, personal communication, June 2021), providing a second avenue by which stalling may

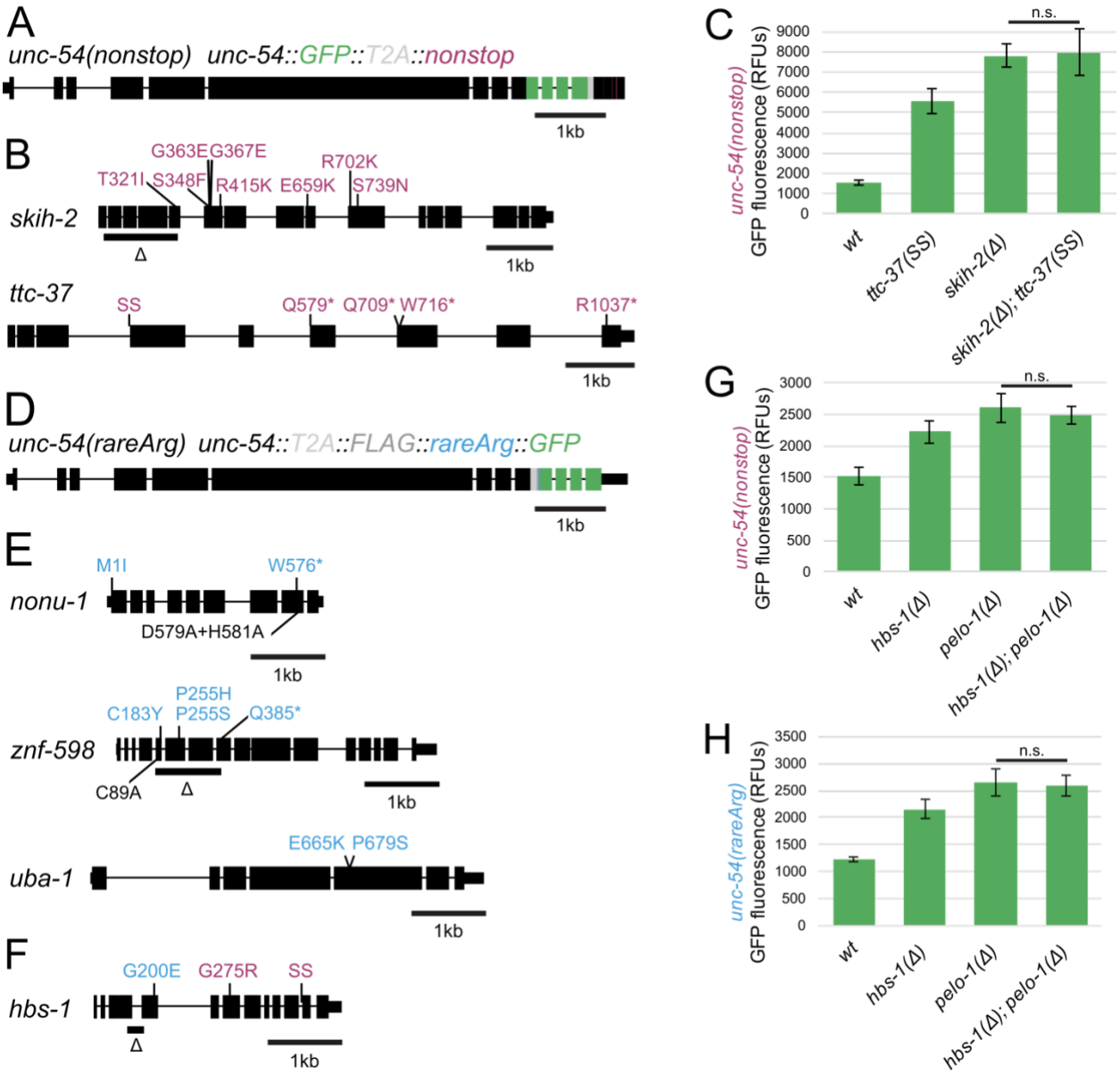

Figure 1. Nonstop and No-Go mRNA Decay suppressors identified via genetic screens. (A) Gene diagram showing annotated exons (black rectangles) of *unc-54(nonstop).* Colored rectangles represent CRISPR/Cas9 insertions at the endogenous *unc-54* locus: GFP (green), T2A sequence (grey), and no stop codons (burgundy). **(B)** Diagrams of *skih-2* and *ttc-37* alleles. Black rectangles represent exons, thicker rectangles are CDS, and thin lines are introns. Mutations made via EMS in the Nonstop mRNA Decay screen (burgundy) and via CRISPR/Cas9 are above and below the gene, respectively. **(C)** Mean relative fluorescence units (RFUs) of indicated strains in the *unc-54(nonstop)* background. One standard deviation shown as error bars. p values from Student's t-test. **(D)** Gene diagram showing annotated exons (black rectangles) of *unc-54(rareArg).* Colored rectangles represent CRISPR/Cas9 insertions at the endogenous *unc-54* locus: T2A sequence (grey), FLAG (dark grey), 12 rare arginine codons (blue), and GFP (green). **(E)** *znf-598*, *nonu-1*, and *uba-1* alleles drawn as in part (B). Mutations made via EMS in the rareArg screens (blue) and via CRISPR/Cas9 are above and below the gene, respectively. **(F)** *hbs-1* alleles drawn as in part (B). Nonstop EMS mutations (burgundy) and a rareArg EMS mutation (blue) are above the gene. A deletion made by CRISPR/Cas9 is below. **(G)** Mean RFUs of indicated strains in the *unc-54(nonstop)* background. **(H)** Mean RFUs of indicated strains in the *unc-54(rareArg)* background.

occur. Strains with the *unc-54(rareArg)* construct and functional No-Go mRNA Decay machinery showed impaired movement and exhibited very low levels of GFP, supporting a model where mRNAs from this locus are targeted by No-Go mRNA Decay.

To validate the *unc-54(rareArg)* reporter, we crossed it with alleles of two factors known to be required for No-Go mRNA Decay: *znf-598* and *nonu-1* (Brandman et al., 2012; Juszkiewicz & Hegde, 2017; Sundaramoorthy et al., 2017; D'Orazio et al., 2019; Glover et al., 2020). In each case we observed de-repression of the reporter, manifest as increased fluorescence and an improvement in animal movement and egg laying. The *nonu-1* result is consistent with our prior work showing that this stretch of twelve rare arginine codons confers *nonu-1*-dependent mRNA decay (Glover et al., 2020). Given that most of our mechanistic understanding of No-Go mRNA Decay comes from work in *S. cer* (Doma and Parker, 2006; Simms et al., 2017; D'Orazio et al., 2019), and that genetic screens in human K562 cells have failed to identify the NONU-1 homolog (Hickey et al., 2020), we reasoned a genetic screen in *C. elegans* would prove insightful and augment information gained from other systems. Using *unc-54(rareArg),* we performed two genetic screens (Methods). Here we report nine alleles in No-Go mRNA Decay machinery (Fig 1E, Fig 1F).

Eight alleles were split amongst three readily-identifiable No-Go mRNA Decay components: *nonu-1, znf-598,* and *uba-1*. We found two mutations in *nonu-1*, as would be expected based on the *unc-54(rareArg)* reporter validation. We isolated four mutations in *znf-598*, three of which were missense mutations. One mutation, C183Y, is within a region that matches the consensus for a C2H2 zinc finger in *C. elegans* and *H. sapiens,* but is not conserved in *S. cer.* Two alleles at P255 (P255S, P255H) mutated the highly conserved GHP motif at the start of a C2H2 zinc finger. We also identified two mutations in *uba-1*, the sole E1 ubiquitin-activating enzyme in *C. elegans*. Both *uba-1* mutations (E665K, P679S) exhibited poor viability, as would be expected as complete loss of *uba-1* is thought to be lethal (Kulkarni, et al., 2008). We confirmed the *uba-1* result by crossing in a known temperature-sensitive loss-of-function allele of this gene (*it129*), and observed the expected temperature-dependent de-repression of GFP. As ZNF-598 is known to function in other systems as a ubiquitin ligase (Juszkiewicz & Hegde, 2017; Sundaramoorthy et al., 2017), we expect that *uba-1* loss-of-function compromised the Ub-conjugation cascade, giving rise to *unc-54(rareArg)* de-repression.

Requirement for ribosome rescue in both Nonstop mRNA Decay and No-Go mRNA Decay

Among the factors hit in Nonstop and No-Go mRNA Decay screens was *hbs-1,* with two alleles from the Nonstop mRNA Decay screen and one allele from the No-Go mRNA Decay screen. Requirement of *hbs-1* in both pathways was confirmed by crossing in a deletion allele constructed by CRISPR/Cas9. Interestingly, two mutations from the screens hit GTP-binding and active site residues (G200E in No-Go mRNA Decay, G275R in Nonstop mRNA Decay), consistent with a functional requirement for GTP binding and hydrolysis by HBS-1 in both pathways. As HBS-1 homologs are known to function in a complex with PELO-1 homologs, we also tested whether *pelo-1* is required for both pathways. In *hbs-1* and *pelo-1* mutants, we observed consistent de-repression of *unc-54(nonstop)*, and a similar pattern in *unc-54(rareArg)*. Interestingly, in both reporters the effect of *hbs-1* was slightly less than the effect of *pelo-1*, suggesting PELO-1 may have some residual activity in the absence of HBS-1, as might be expected given PELO-1's direct role in A-site recognition (Pisareva et al., 2011; Shoemaker & Green 2011). In agreement with the idea that PELO-1 and HBS-1 function together, the double mutants (*hbs-1 pelo-1)* for both reporters were similar to the *pelo-1* mutant (Fig 1G, Fig 1H).

Exosome divergence at the Ski7 interface in *C. elegans*

Despite the success of our genetic screens, homologs of two conserved SKI complex components (Ski7 and Ski8) remain unidentified in *C. elegans*. Sequence homology searches using either *S. cer* Ski8 or *H. sap* WDR61 identified six homologs in *C. elegans* (*wdr-5.1*, *wdr-5.2*, *wdr-5.3*, *lis-1*, *pfs-2*, *sel-10*). All but PFS-2 exhibited conservation of residues known to be important for the *S. cer* Ski2-Ski8 interface (HxD, REF Halbach et al. 2013 23953113). Thus, genetic redundancy seems a plausible explanation for the lack of loss-of-function mutations in Ski8 homologs from the screen.

We also attempted to understand why a Ski7 homolog was not identified in our screen. Ski7 proteins exhibit little sequence conservation outside of a short "S3 motif" FXX[P/A]SPD[D/E] conserved in all known Ski7 homologs (Fig 2) (Marshall et al., 2018). Prior work using this motif failed to identify a Ski7 homolog in *C. elegans* (Marshall et al., 2018). We also performed sequence homology searches with both conventional and custom-built software (see Methods), and failed to identify a Ski7 homolog with the S3 motif. Given this result, we conducted additional homology searches using lesser conserved motifs from Ski7 homologs (see Methods). While we did identify a single gene with N-terminus identical to some Ski7 homologs

(M[A/S]RHR), a deletion spanning much of this gene failed to yield a phenotype in our *unc-54(nonstop)* reporter (Fig S2).

We considered the possibility that Ski7 function may be encoded via alternative splicing of the *hbs-1* gene as it is in several organisms; however, neither of the *hbs-1* isoforms contain an S3-motif. We looked for additional *hbs-1* isoforms by analyzing RNA-seq and nanopore sequencing (Roach et al., 2020), but failed to identify anything more than the two annotated *hbs-1* isoforms. In agreement with this logic, our *hbs-1* deletion exhibited a phenotype similar to *pelo-1* mutations, not *skih-2* nor *ttc-37* mutations. We thus conclude that Ski7 is not encoded by the *hbs-1* gene in *C. elegans*.

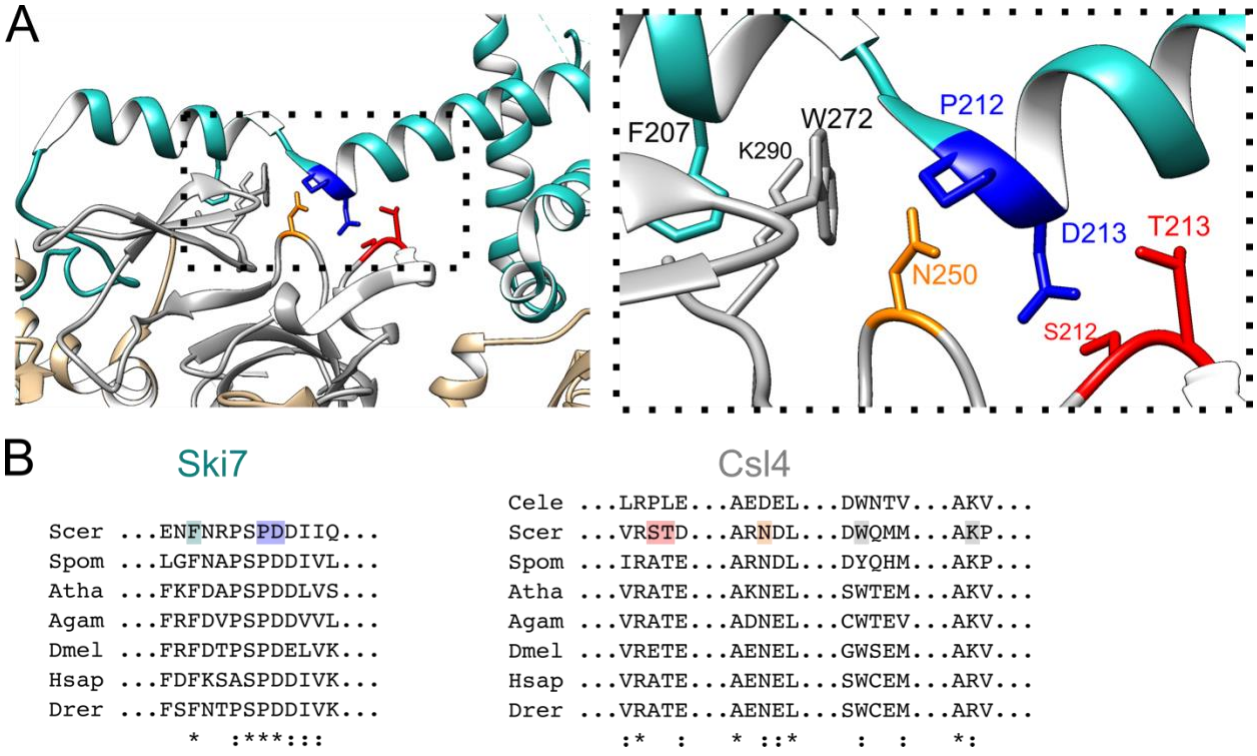

Figure 2. Exosome divergence at the Ski7 interface in *C. elegans*. (A) Structure of Ski7 (teal) bound to Csl4 (grey), focused on the S3 motif of Ski7. Structure from *S. cerevisiae* (Kowalinski et al., 2016). Dotted line indicates region of focus on right. Residues are colored to facilitate comparison with multiple sequence alignment, and numbered per *S. cer*. **(B)** Multiple sequence alignment of Ski7 and Csl4 proteins from several species, highlighting conservation of residues at the Ski7-Csl4 interface. Note conservation and divergence of some sequences in *C. elegans*; see text for further details. Species are as follows: Cele (*Caenorhabditis elegans*), Scer (*Saccharomyces cerevisiae*), Spom (*Schizosaccharomyces pombe*), Atha (*Arabidopsis thaliana*), Agam (*Anopheles gambiae*), Dmel (*Drosophila melanogaster*), Hsap (*Homo sapiens*), Drer (*Danio rerio*). Conservation below alignments is as follows: asterisks indicate identity, colons indicate amino acids with strongly similar properties, periods indicate amino acids with weakly similar properties.

We sought to reconcile the apparent absence of a Ski7 sequence homolog in *C. elegans* despite an active Nonstop mRNA Decay pathway. The S3 motif is required for interaction between Ski7 and the exosome subunit (Csl4) and also Nonstop mRNA Decay function (Fig 2A, REF Kowalinski et al., 2016 27345150; van Hoof et al., 2000 11027292). We thus examined the sequence of Csl4 homologs across eukarya. In virtually all species examined, the residues of Csl4 that interact with Ski7 are conserved, with the exception of *C. elegans* and related invertebrates (Fig 2B). Given the divergence of the exosome interface with which the Ski7 S3 motif interacts, there is no expectation that the S3 motif would be conserved. The remainder of the Ski7-exosome interface is composed of hydrophobic interactions and exhibits no recognizable sequence conservation (Kalisiak et al., 2017; Kowalinski et al., 2016). While this logic does explain the absence of a Ski7 sequence homolog, it does not explain why our genetic screen did not identify a Ski7 functional homolog (see Discussion).

mRNA decay is a major downstream consequence of ribosomal ubiquitination by ZNF-598

In the No-Go mRNA Decay screen, we recovered several alleles of *znf-598*. ZNF-598 homologs are known to recognize ribosomal collisions and ubiquitinate sites on the small subunit, including RPS-10 (eS10) and RPS-20 (uS10) (Juszkiewicz & Hegde, 2017; Sundaramoothy et al., 2017). By multiple sequence alignment, we identified a catalytic Cys (C89) (Sundaramoorthy et al., 2017) known to be required for Ub conjugation to substrates of Hel2/ZNF598 (Fig 3A), and generated a point mutation (C89A) via CRISPR/Cas9. In an immunoblot, we observed a shift to the expected size for Ub-RPS-10 which depended on the catalytic activity of ZNF-598 (Fig 3B). The *znf-598(C89A)* mutant phenocopied the deletion of *znf-598* (Fig 3C), consistent with the idea that ZNF-598 requires its ubiquitin ligase domain for No-Go mRNA Decay repression. Taken together, these results support ZNF-598 repressing No-Go mRNAs via ribosomal ubiquitination in *C. elegans*, as is thought to occur in other systems.

Prior work has underscored the importance of ribosomal ubiquitination events in No-Go mRNA Decay. However, the precise functional contributions of individual ubiquitination sites has remained unclear, in part due to the difficulty in obtaining viable mutants in the relevant ribosomal proteins. Our system (*C. elegans*) seemed well-suited to address this question. We therefore generated single and double-mutant combinations of *znf-598* along with its targets, then measured the effect on the *unc-54(rareArg)* reporter. Mutants of the ubiquitination sites on RPS-10 and RPS-20 exhibited a mild de-repression of the reporter, consistent with both sites

contributing to stalling-induced repression (Fig S3, Fig 3D). Simultaneous knockout of ubiquitination sites on RPS-10 and RPS-20 generated a comparable de-repression to that observed in the *znf-598* mutant. Furthermore, an *rps-10 znf-598* double mutant phenocopied the de-repression observed in the *znf-598* single mutant. Based on these results, we conclude that ZNF-598 must ubiquitinate at least RPS-10 on the ribosome, and RPS-10 and RPS-20 must both be ubiquitinated to elicit full repression during No-Go mRNA Decay.

Having established a requirement for ubiquitination by ZNF-598 in this system, we decided to investigate the relationship of ubiquitination to mRNA decay. A key effector of No-Go mRNA Decay is NONU-1, an endonuclease with Ub-binding domains identified in our screen (Fig 1E), which was also identified in our prior Nonstop mRNA Decay screen (Glover et al., 2020). We hypothesized that ZNF-598 deposits ubiquitin on stalled ribosomes during No-Go mRNA Decay to recruit NONU-1 and elicit mRNA cleavage. To test this model, we combined mutations in *znf-598* and its targets with *nonu-1(AxA)*, a catalytic mutation of *nonu-1* that phenocopies a deletion in *nonu-1* (Glover et al., 2020). A *znf-598 nonu-1* double mutant phenocopied a *znf-598* single mutant, which is in agreement with NONU-1 acting downstream of ubiquitination by ZNF-598 (Fig 3E). Interestingly, the magnitude of *unc-54(rareArg)* de-repression in a *nonu-1* single mutant differed from that observed in either *rps-10* or *rps-20* mutant. Moreover, an *rps-10 nonu-1* double exhibited greater reporter de-repression than either single mutant. Taken together, these results indicate that NONU-1 functions downstream of ZNF-598 in No-Go mRNA Decay, though does not strictly rely on either RPS-10 or RPS-20 ubiquitination. Consistent with this model, we observed an increase of the *unc-54(rareArg)* reporter mRNA in *znf-598*, indicating that mRNA destabilization is a major downstream consequence of ZNF-598 (Fig 3F).

To determine if the relationship between ZNF-598 and NONU-1 is a broadly conserved phenomenon, we performed phylogenetic profiling. Briefly, phylogenetic profiling scores pairs of proteins using mutual information, which can be interpreted as the tendency of the protein pair to function together, either redundantly or sequentially. High mutual information can be achieved when two proteins are inherited together or lost together, or when two proteins are genetically redundant and at least one protein is maintained (reviewed in Dey and Meyer 2015). We carried out phylogenetic profiling by searching 111,921 profile HMMs (Mi et al., 2021) on genomic and transcriptomic sequences from 473 protists as these represent diverse eukaryotic lifestyles (see Methods). To validate this approach, we calculated mutual information between pairs of factors known to function together in a complex, such as LTN-1/RQC-2 and PELO-1/HBS-1 (Fig S4)

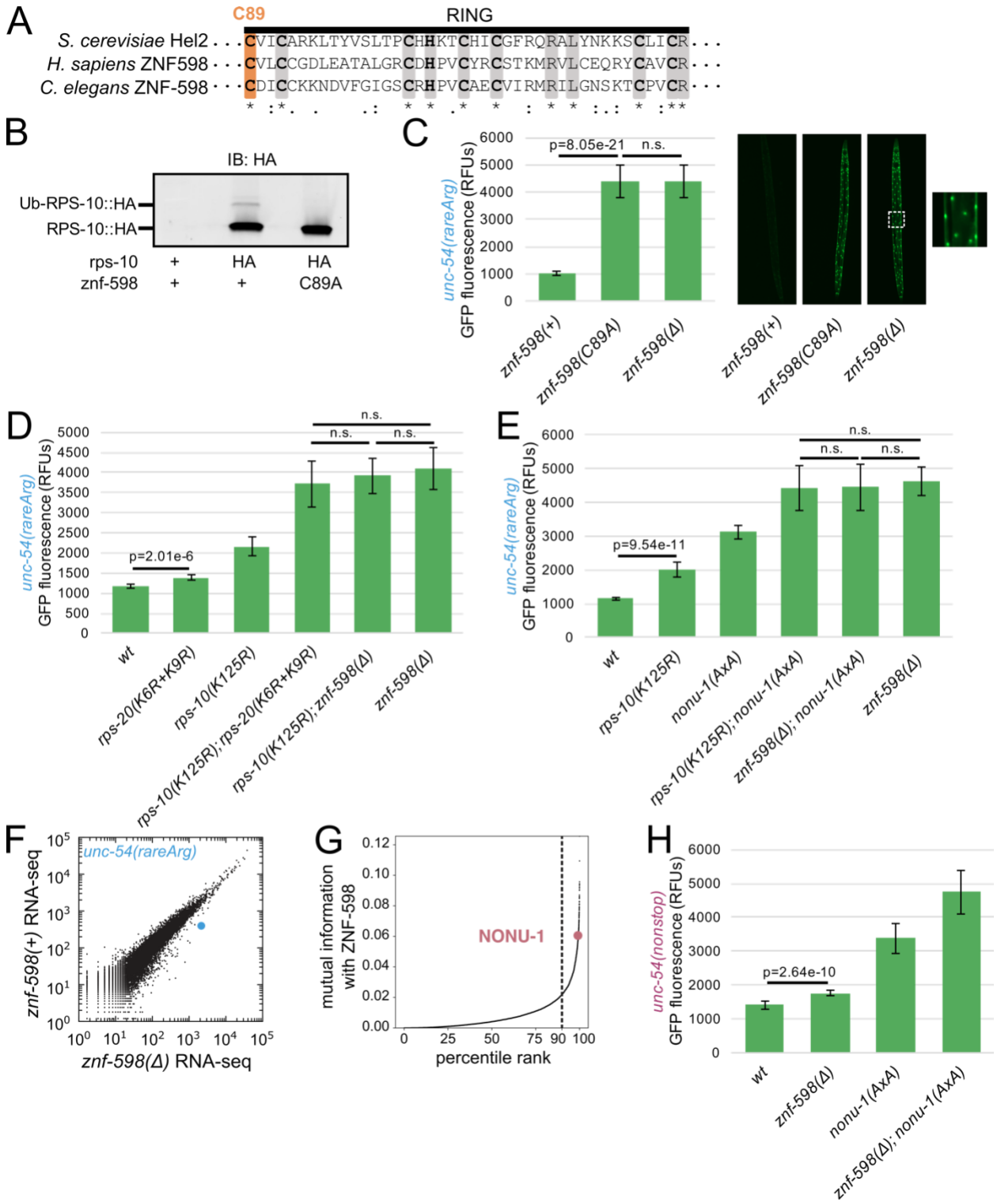

Figure 3. mRNA decay is a major downstream consequence of ribosomal ubiquitination by ZNF-598. (A) Multiple sequence alignment of *S. cer* Hel2, *H. sapiens* ZNF598, and *C. elegans* ZNF-598 RING finger domain. Conserved residues are in grey and C89 in orange. Conservation is as shown in Fig 2B. **(B)** Western blot of indicated strains to monitor ubiquitination of HA-tagged RPS-10. **(C)** Mean RFUs of indicated strains in the *unc-54(rareArg)* background, with representative images at right. Zoom in shows nuclear localization of GFP. One standard deviation shown as error bars. p values from Student's t-test. **(D, E)** Mean RFUs of indicated strains in the *unc-54(rareArg)* background. **(F)** Genome-wide RNA-seq of the indicated strains. All genes are shown as black dots and *unc-54(rareArg)* in blue. **(G)** ZNF-598 mutual information plot. 90% percentile cutoff is shown as a dashed line and NONU-1 is highlighted in pink. See Methods. **(H)** Mean RFUs of indicated strains in the *unc-54(nonstop)* background.

(Kostova et al., 2017; Shoemaker et al., 2010; Becker et al., 2011; Hilal et al., 2016). LTN-1/RQC-2 and PELO-1/HBS-1 exhibited high mutual information, scoring in each others' top 99.88% (PELO-1 ranked 19th of 15,909 interactions with HBS-1) and 98.86% (RQC-2 ranked 181th of 15,909 interactions with LTN-1), respectively. Similarly, we observed that ZNF-598 and NONU-1 ranked in each others' top 99.38% (NONU-1 ranked 99th of 15,909 interactions with ZNF-598) (Fig 3G). Thus ZNF-598 and NONU-1 are a broadly conserved functional pair across diverse eukaryotes, with our work in *C. elegans* suggesting that this pair functions in No-Go mRNA Decay to degrade No-Go mRNAs.

We were curious to determine whether *nonu-1* function depends on *znf-598* in Nonstop mRNA Decay as well. Thus, we quantified their effects on the *unc-54(nonstop)* reporter (Fig 3H). In contrast to its strong effect on the *unc-54(rareArg)* reporter, the *znf-598* mutant showed mild *unc-54(nonstop)* de-repression. These results are consistent with a more modest role for *znf-598* in Nonstop mRNA Decay than that observed at *unc-54(rareArg)*, and explains why our Nonstop mRNA Decay screens failed to identify *znf-598* (Arribere and Fire, 2018; Glover et al., 2020). Surprisingly, *nonu-1* exhibited a greater de-repression of *unc-54(nonstop)* than *znf-598*, and the double mutant expressed higher levels of GFP than either single mutant. The fact that *nonu-1* and *znf-598* together exhibit additive effects suggests that NONU-1 is recruited via an E3 ubiquitin ligase other than ZNF-598 during Nonstop mRNA Decay.

Structural, computational, and functional evidence for ubiquitin-binding by HBS-1

Several of our No-Go mRNA Decay suppressors (*znf-598*, *nonu-1*, *uba-1*) encoded factors involved in Ub-dependent processes, so we were initially surprised that this screen also identified the ribosome rescue factor *hbs-1*. We therefore examined HBS-1 to determine whether it could conceivably function in a Ub-dependent manner.

The HBS-1 protein consists of an N-terminal domain, a disordered linker region, a GTPase domain, and two beta-barrel domains (Becker et al., 2011; Hilal et al., 2016). We noticed that the N-terminal domain of HBS-1, while poorly conserved at the sequence level, adopts a distinct triple helix fold that is classified by Pfam as a member of the ubiquitin-binding Uba clan (Fig 4A). Notable members of the Uba clan include the Uba and Cue domains, found in *S. cer* Rad23 and *C. elegans* NONU-1, respectively. In light of this structural homology, we scrutinized the arrangement of surface-exposed residues in the *S. cer* Hbs1 N-terminus and noticed similar amino acids at sites known to be important for the Uba-Ub interaction. Ub-binding domains are

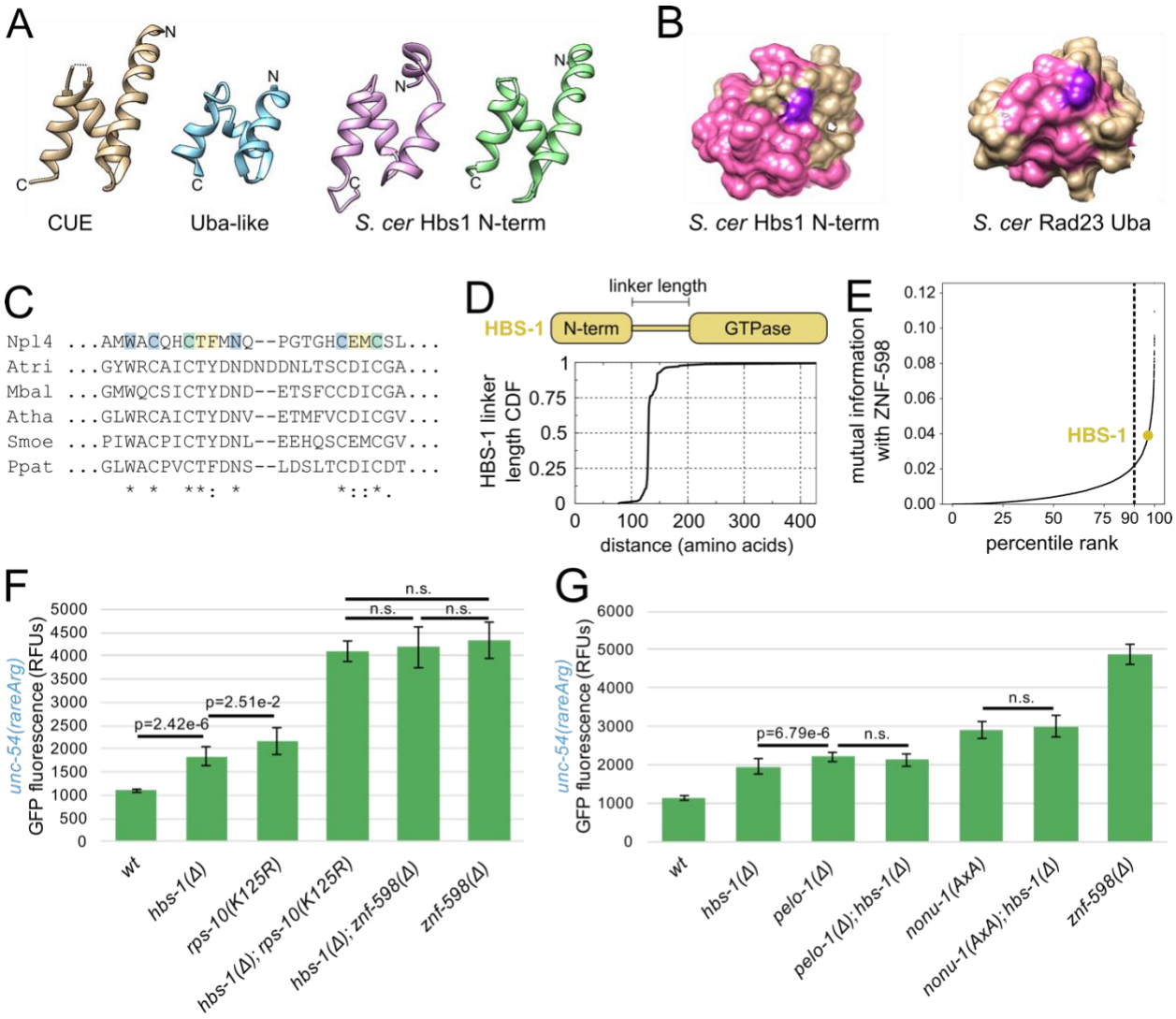

Figure 4. Structural, computational, and functional evidence for ubiquitin-binding by HBS-1. (A) Structural homology between Hbs1 N-terminal domain and ubiquitin-binding domains. Shown are structures representative of the UBA clan: CUE (tan, *S. cer* Vps9p, 1P3Q, [Prag et al., 2003]) and Uba-like (blue, *S. cer* Dcn1, 2L4E, [Burschowsky et al., unpublished]). At right are two structures of the Hbs1 N-terminus from (Becker et al., 2011) (pink, 3IZQ) and (Hilal et al., 2016) (green, 5M1J). Amino and carboxy termini indicated with N and C, respectively. Note overall similarity in topology and fold across all four structures. **(B)** Structural surface depiction of the *S. cer* Hbs1 N-terminal domain (left, 3IZQ) and Rad23 Uba domain (right, 2QSF). Three alpha helices are aligned in the same orientation, consisting of amino acids 20-83 of Hbs1 and 354-395 of Rad23. Hydrophobic residues are highlighted in pink, glycine in purple, and other residues in beige. **(C)** The N-terminal ZnF of plant Hbs1 is homologous to the Ub-binding ZnF of rat Npl4. Multiple sequence alignment of the Zinc Finger (ZnF) of Hbs1 from phylogenetically diverse plants. Residues that are highly conserved among Npl4 homologs are in blue, residues that contact Ub are in yellow, and residues that are both conserved and contact Ub are in green. Coloring and annotation of Npl4 residues from (Alam et al., 2004). Species are Atri (*Amborella trichopoda*), Mbal (*Musa balbisiana*), Atha (*Arabidopsis thaliana*), Smoe (*Selganiella moellendorffii*), and Ppat (*Physcomitrium patens*). **(D)** Top: Diagram of HBS-1 domain architecture. Bottom: Cumulative distribution function (CDF) of HBS-1 linker length in 177 orthologs of human HBS1L. Values calculated by subtracting the 3' end of the HBS-1 N-terminus domain from the 5' end of the GTPase domain. Domain bounds were determined by pfam and Hmmer. One data point was cropped from the graph along the X-axis with a linker length of 428 amino acids. See Methods. **(E)** ZNF-598 mutual information plot. 90% percentile cutoff is shown as a dashed line and HBS-1 is highlighted in yellow. **(F, G)** Mean RFUs of indicated strains in the *unc-54(rareArg)* background.

notable in their absence of substantial sequence identity (reviewed in Randles and Walters, 2012), an emergent property of the hydrophobic interface with Ub, providing an explanation for the low sequence identity among HBS-1 N-termini. Despite low sequence conservation, prior work identified a glycine surrounded by surface-oriented hydrophobic residues as a unique characteristic of Uba domains (Mueller and Feigon, 2002). This feature is shared with the Hbs1 N-terminus domain, supporting a Ub-binding role for HBS-1 N-termini (Fig 4B). We also noticed that plant HBS-1 homologs contain a conserved C4-type zinc finger homologous to a known Ub-binding domain from rat (Fig 4C) (Alam et al., 2004). Thus, we hypothesize that the Ub-binding function of HBS-1 emerged relatively early in the evolution of this factor. Taken together, these observations support the idea that HBS-1's N-terminus binds ubiquitin, and that this feature is broadly conserved across species.

To understand the role that Ub-binding might play in HBS-1 function, we analyzed cryo-EM structures of yeast HBS-1 bound to ribosomes stalled on Nonstop and No-Go mRNA Decay reporters. In both structures, the HBS-1 N-terminus is bound to the 40S subunit near uS10 and uS3 (Hilal et al., 2016; Becker et al., 2011). uS10 is an established target of ZNF598/Hel2 in both mammals and yeast, while uS3 is a substrate for ubiquitination in yeast (Juszkiewicz & Hegde, 2017; Sundaramoorthy et al., 2017, Ikeuchi et al., 2019). We hypothesized that the HBS-1 N-terminus recruits the protein to stalled, ubiquitinated ribosomes, thereby allowing the GTPase domain to carry out ribosome rescue.

As an initial evaluation of our model, we carried out two computational analyses. First, if HBS-1 needs to bind the ubiquitination sites on the 40S subunit and PELO-1 simultaneously, we reasoned there would be a conserved minimum linker length connecting the N-terminus domain and the GTPase domain. Consistent with this, an analysis of 177 HBS-1 homologs identified a conserved length of ~130 amino acids, with no homologs below a linker length of 76 amino acids (see Methods) (Fig 4D). This is an ample linker to span the distance from the ubiquitination sites near the mRNA entry tunnel to the A-site (~100Å, ~50 amino acids, measured from Hbs1-bound ribosome structure 5M1J). Second, we examined the coevolution of HBS-1 with ZNF-598 homologs, and observed a relatively high level of mutual information suggesting that HBS-1 and ZNF-598 function together throughout eukarya (Fig 4E).

Our genetic analyses substantiated the notion that HBS-1 functions through ubiquitin binding. Specifically, we observed *znf-598* and *nonu-1* are both epistatic to *hbs-1* (Fig 4F, Fig 4G).

Taken together, our structural, computational, and genetic observations support the idea that ubiquitination is critical for ribosome rescue by HBS-1.

Deletion of ZNF-598 increases mRNA levels of and ribosomes on a No-Go mRNA Decay substrate

Given our genetic evidence placing *znf-598* function upstream of both mRNA decay (via NONU-1) and ribosome clearance (via HBS-1), we were curious to investigate the distribution of ribosomes on *unc-54(rareArg)* with and without ZNF-598. To this end, we performed 28-30nt monosome and 50-62nt disome Ribo-seq with and without *znf-598* deletion (Ingolia et al., 2009; Meydan et al., 2020; Han et al., 2020; Arpat et al., 2020; Zhao et al., 2021) (Fig 5, Fig S5). Consistent with the stabilization of *unc-54(rareArg)* seen by RNA-seq, we observed an increase in both monosome and disome footprints on the reporter in *znf-598(Δ)* (Fig 5A). Within each background, we found that monosome footprints were in agreement with disome footprints on the reporter, indicating that monosome footprint count is a reasonable predictor of the abundance in the captured disomes (Fig 5B).

We sought to determine whether the increase in ribosome footprints in *znf-598(Δ)* was simply the result of increased mRNA levels or whether there were additional *znf-598*-dependent effects on ribosome footprint counts. We calculated the change in ribosome footprints per RNA-seq reads between wildtype and *znf-598(Δ)* and observed strong agreement between mRNA levels and monosome density on *unc-54(rareArg)* (Fig 5C, Fig 5D). In accordance with the similar amounts of monosome and disome footprints, we observed similar agreement between mRNA levels and disome density. These data indicate that the increase in ribosomes on *unc-54(rareArg)* in *znf-598(Δ)* is largely explained by the increase in mRNA levels. Interestingly, we note that monosome footprints in wildtype and *znf-598(Δ)* were enriched in the 5' end of the mRNA (Fig 5E, Fig S6). This result could emerge from increased ribosome loading on No-Go mRNAs, ribosome drop-off during elongation, or both.

We next drew our attention to the distribution of ribosomes along our reporter. In considering ribosome position, it is important to understand that--while affected by mRNA levels--*unc-54(rareArg)* is primarily a readthrough reporter. Ribosomes are required to translocate through the rareArg stretch, and their success in completing this feat allows for GFP expression. Evidence of stall readthrough and post-T2A production of FLAG::polyArg::GFP is visible by the nuclear localization of GFP when de-repressed (Fig 3C). This observation revealed our serendipitous construction of an N-terminal motif (a run of arginines) matching the sequence

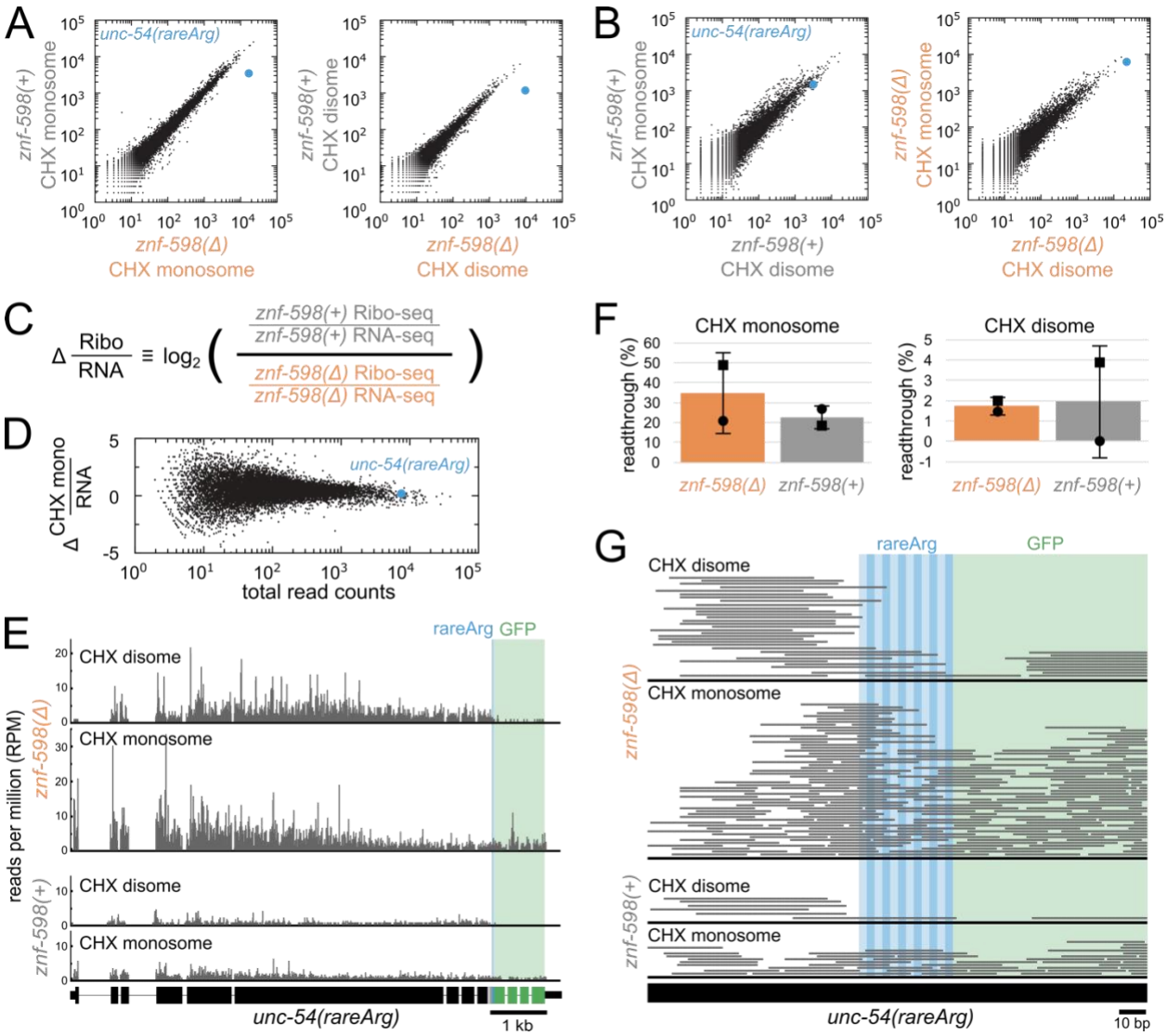

Figure 5. Deletion of ZNF-598 increases mRNA levels of and ribosomes on a No-Go mRNA Decay substrate. **(A)** Rocket plots of CHX monosome and disome Ribo-seq reads per million (RPM) in *znf-598(+)* vs. *znf-598(Δ)*. All genes are shown as black dots and *unc-54(rareArg)* is highlighted in blue. **(B)** As in (A), comparing CHX monosome vs. disome Ribo-seq RPM within one background. **(C)** Equation used to calculate the change in ribosome footprints per mRNA reads. Log change score is determined by dividing Ribo-seq read counts by RNA-seq read counts in each background, then dividing values for *znf-598(+)* by values for *znf-598(Δ)*. **(D)** Dot plot showing the change in ribosome footprints per mRNA reads between *znf-598(+)* and *znf-598(Δ)* CHX monosome libraries. Y-axis position is the change score as calculated by the equation in (C). A more positive score indicates fewer monosome Ribo-seq read counts normalized to RNA-seq in *znf-598(Δ)*; a more negative score indicates fewer monosome Ribo-seq read counts normalized to RNA-seq in *znf-598(+)*. X-axis position is the total number of read counts in all libraries. All genes are shown as black dots and *unc-54(rareArg)* is highlighted in blue. **(E)** Gene plot showing CHX disome (50-62nt) and monosome (28-30nt) Ribo-seq RPM on *unc-54(rareArg)* in *znf-598(Δ)* and *znf-598(+)*. Reads are aligned by their 5' ends. Locations of 12 rare arginine codons (blue) and GFP (green) are annotated. **(F)** Percentage of readthrough CHX monosome (28-30nt) footprints (left) and CHX disome (50-62nt) footprints (right) on *unc-54(rareArg)* in indicated backgrounds from two biological replicates. Data points from replicate one are shown as black circles and replicate two are shown as black squares. One standard deviation shown as error bars. See Methods. **(G)** Pile up of CHX disome (50-62nt) and monosome (28-30nt) Ribo-seq reads around rareArg in the indicated backgrounds. Each arginine codon is represented by a vertical blue stripe. Each bar represents one read. Monosome datasets and disome datasets are subsampled to equal depth across the two backgrounds.

requirements for a nuclear localization signal (Lu et al., 2021; Davis et al., 2021).

Given that GFP production from *unc-54(rareArg)* relies on readthrough, we hypothesized that some population of ribosomes must escape the stall and evade clearance. Indeed, we observed that monosome density downstream of the stall was 18-49% the level seen prior to the stall, with at most a mild effect by *znf-598(Δ)* on this metric (Fig 5F). The reduction in footprints downstream of the stall persisted in disomes (Fig 5F). We conclude that ZNF-598 does not dramatically alter the relative number of ribosomes upstream versus downstream of the stall.

Prior work in certain yeast mutants have observed frameshifting on No-Go mRNAs (Wang et al., 2018; Simms et al., 2019). We considered frameshifting as a mechanism by which ribosomes may pass through the arginine stall. Within and downstream of the stall, we detected no significant change in frame in ribosome footprints in either wild type or in *znf-598(Δ)* animals, in agreement with yeast data on an arginine reporter (Fig S7A) (D'Orazio et al., 2019). As a second way of assessing the contributions of frameshifting to expression of *unc-54(rareArg)*, we examined expression in a *smg-1* mutant which has a nonfunctional Nonsense-mediated mRNA Decay pathway. Ribosomes that frameshift would be expected to terminate at an out-of-frame stop codon just past the arginine stall and trigger Nonsense-mediated mRNA Decay. We observed no increase in reporter expression in a *smg-1* mutant (Fig S7B). Taken together, these results argue against frameshifting as a substantial contributor to the expression of *unc-54(rareArg)*. We note these results are not surprising given that Mbf1 was intact in our experiments; Mbf1 is known to enhance frame maintenance at stalls (Wang et al., 2018).

Considering the requirement of polyArg synthesis to produce GFP, we were surprised to see few ribosomes decoding the rareArg stretch (Fig 5G). The low abundance of footprints in this region was notably independent of mapping error; the arginine codons we selected were arranged in a non-random order to enable unique read-mapping. In agreement with our results on *unc-54(rareArg)*, we observed a depletion of ribosomes decoding poly-basic sites genome-wide, independent of a nucleotide capture bias (Fig S8, Fig S9). While in contrast to datasets made in *S. cer* (Meydan et al., 2020; D'Orazio et al., 2019; Zhao et al. 2021), this observation is consistent with multiple *C. elegans* datasets (Stadler and Fire, 2011; Glover et al., 2020), human and zebrafish data (Han et al., 2020), and mouse data (Arpat et al., 2020) made using the elongation inhibitor cycloheximide (CHX).

Ribo-seq libraries lack accumulations at arginine stalls

In an effort to identify a stall-decoding species, we performed 18-30nt monosome Ribo-seq and 40-60nt disome Ribo-seq utilizing anisomycin (ANS) rather than cycloheximide (CHX) (Fig S10, Methods). CHX inhibits translocation by binding the E-site and preventing deacylated tRNAs from exiting the P-site. Thus, CHX stabilizes ribosomes in a hybrid, pre-translocation state (Fig 6A). ANS inhibits peptide-bond formation by binding the A-site and competing with aminoacyl-tRNAs for the peptidyl transferase center (reviewed in Dmitriev et al., 2020). Previous studies have used ANS to stabilize ribosomes with short 21nt footprints (Lareau et al., 2014). These ribosomes are expected to be in a classical state with either an empty A-site (pre-accomodation) or a free tRNA in their A-site (pre-peptidyl transfer) (Fig 6A). Given the expectation for slow accommodation at rare codons, we investigated whether ANS-dependent footprints resided in our arginine stretch.

Surprisingly, we captured both 21nt and 28nt monosome footprints via ANS, in contrast to ANS work done in yeast which captured very few 28nt footprints (Fig S10) (Lareau et al., 2014). We utilized this feature to probe the positions of multiple ribosome species on our reporter. Given the rarity of their cognate tRNAs, we expected the 12 rare arginine stretch to stall ribosomes with empty A-sites. However, we observed few ANS-stabilized monosome footprints (21nt or 28nt) within the stall, and even more footprints immediately following the stall (Fig 6B, Fig 6C). To further investigate this phenomenon, we considered the possibility that arginine-decoding ribosomes exist as disomes rather than monosomes.

To this end, we captured a wide range of in-frame disome species using ANS: 42-48nt, 51nt-54nt, and 58-62nt (Fig 6A, Fig S10). We expect that the two smaller species lacking from CHX disome libraries represent events when both ribosomes are in the classical state (42-48nt), or one ribosome is in the classical state with the other in the hybrid state (51-54nt). Despite our capture of additional species via ANS, monosomes remained a general predictor of disome counts (Fig S11). Additionally, we observed a depletion of ribosomes within the 12 arginines on *unc-54(rareArg)* (Fig 6B, 6C). Consistent with these results on our reporter, we found a depletion of monosomes and disomes at arginine codons genome-wide (Fig 6D). Taken together, we propose that standard monosome and disome Ribo-seq protocols are unable to capture metazoan ribosomes at strong stalls. Future work will address the novel molecular features of these ribosomes and optimize their capture.

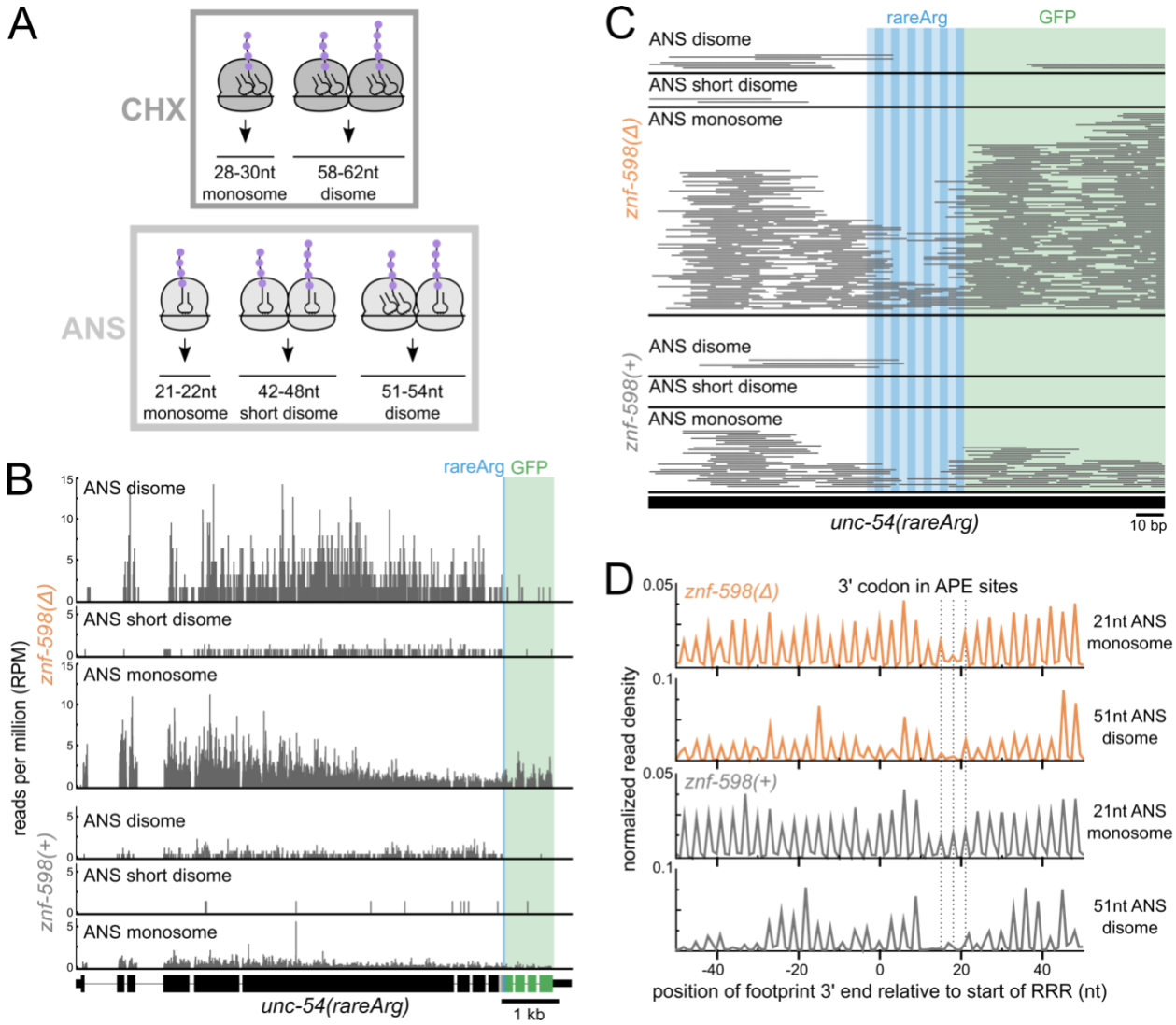

Figure 6. Ribo-seq libraries lack accumulations at arginine stalls. (A) Ribosome conformations and footprint sizes with cycloheximide vs. anisomycin. **(B)** Gene plot showing ANS disome (50-62nt) and monosome (18-30nt) Ribo-seq RPM on *unc-54(rareArg)* in *znf-598(Δ)* and *znf-598(+)*. Reads are aligned by their 5' ends. Locations of 12 rare arginine codons (blue) and GFP (green) are annotated. **(C)** Pile up of ANS disome (50-62nt) and monosome (18-30nt) Ribo-seq reads around rareArg in the indicated backgrounds. Each arginine codon is represented by a vertical blue stripe. Each bar represents one read. Monosome datasets and disome datasets are subsampled to equal depth across the two backgrounds. **(D)** Normalized read density of ANS monosome (21nt) and disome (51nt) Ribo-seq reads genome-wide at RRR amino acid motifs in the indicated backgrounds. Reads are aligned by their 3' ends. Dotted lines indicate the footprint 3' end position when the third R of RRR is in each ribosomal site.

DISCUSSION

Here, we investigated the functions of and interplay between several factors required for Nonstop and No-Go mRNA Decay. Through our Nonstop mRNA Decay system, we identified functionally important residues in the SKI complex and suggested models consistent with exosome-independent mRNA repression (Fig 1, Fig 2). By establishing No-Go mRNA Decay in *C. elegans,* we uncovered NONU-1 and HBS-1 recruitment as a downstream consequence of ribosomal ubiquitination via ZNF-598 (Fig 3, Fig 4). Subsequent work supported a novel Ub-

binding function for the poorly characterized N-terminus of HBS-1. Additionally, our work highlighted ZNF-598's critical role in destabilizing No-Go mRNAs and provided molecular insights into the variety of ribosome species present at stall sites (Fig 5, Fig 6). Our analysis of both Nonstop and No-Go mRNA Decay pathways revealed similarities in their dependencies (*pelo-1*, *hbs-1*, *nonu-1*) and some key differences (*znf-598*).

Architecture and function of the SKI complex in *C. elegans*

Using both genetic screens and sequence homology searches, we have identified functional components of the SKI complex including Ski2 and Ski3. Surprisingly, we did not uncover Ski7 nor Ski8 homologs in *C. elegans*. An approximate calculation suggests that our failure to find Ski7 and Ski8 is not due to insufficient screening: between this and a prior study we recovered 23 mutations in *skih-2* and 7 mutations in *ttc-37* (Fig 1B) (Arribere and Fire, 2018), yielding an average hit rate of 6.05 and 2.09 mutations/kb, respectively. Using even the lower bound of these two genes' mutation frequency, and given the size of yeast Ski8 (~1.2kb) and human Ski7 (~1.8kb), we would have expected at least one loss-of-function mutation in each protein (92% and 98% chance, respectively).

Ski8 is known to be an essential component of the heterotetrameric SKI complex in other systems (Ski2-Ski3-2xSki8). Our screens uncovered two mutations in Ski2 at G363E and G367E, residues that lie near the Ski8 interface, and we thus hypothesize that a Ski8 homolog exists in *C. elegans* (Fig S1). A simple homology search for Ski8 reveals six sequence homologs, suggesting that redundancy may have precluded identification of a functional Ski8. Alternatively, *C. elegans*' Ski8 may have essential functions outside of the SKI complex, as Ski8 is known to moonlight in meiotic recombination in yeast (Arora et al., 2004). Future biochemical analyses may identify which Ski8 homolog(s) function in the *C. elegans* SKI complex.

Our screens also failed to identify a Ski7 homolog. Interestingly, we note that several of the candidate Ski8 homologs contain an unstructured N-terminal extension. We hypothesize that these homologs are fusions of Ski7 and Ski8 function into a single gene. Alternatively (and intriguingly), it is also possible that the *C. elegans* SKI complex functions without a functional Ski7, *i.e.,* that *C. elegans* SKI does not need an association with the 3'>5' exosome to repress its targets. This idea is supported by the observation that the SKI complex alone can extract RNA from ribosomes (Zinoviev et al., 2020). Future work will hopefully clarify the composition and functions of the SKI complex essential to Nonstop mRNA Decay.

Ribosomal ubiquitination as the mechanism for NONU-1 and HBS-1 recruitment

Our work supports a model where both NONU-1 and HBS-1 function downstream of ribosomal ubiquitination by ZNF-598 in No-Go mRNA Decay, though neither effector strictly relies on RPS-10 ubiquitination (Fig 3, Fig 4). What precise ribosomal ubiquitination sites are then recognized by NONU-1 and HBS-1? Existing work is consistent with ribosomal ubiquitination being a central component of No-Go mRNA Decay and highlights the importance of RPS-10 and RPS-20; however, the contributions of each ubiquitination site have remained unclear (Juszkiewicz & Hegde, 2017; Sundaramoorthy et al., 2017).

Here, we conclude that RPS-10 and RPS-20 must both be ubiquitinated to elicit full repression during No-Go mRNA Decay, and we showed that simultaneous knockout of their ubiquitination phenocopied *znf-598*. Our work shows that these sites can function as partially redundant recruitment routes for NONU-1 and HBS-1. Moreover, the level of de-repression in *nonu-1* and *hbs-1* differed from that observed in either *rps-10* or *rps-20*. These data are consistent with a model where RPS-10 or RPS-20 ubiquitination do not act alone in effector recruitment. It is possible that RPS-10 and RPS-20 ubiquitination precede further ubiquitination at other ribosomal sites (Garzia and Meyer et al., 2021 34348161). Surprisingly, an *rps-10 nonu-1* double and an *rps-10 hbs-1* double exhibited greater de-repression than either single mutant. We hypothesize that in lieu of NONU-1 or HBS-1 function, RPS-10 ubiquitination recruits additional factors (such as another endonuclease) to elicit decay of No-Go mRNA Decay substrates (Glover et al., 2020; Navickas et al., 2020). Further genetic work will be required to elucidate the network of ubiquitination sites functioning in No-Go mRNA Decay.

Nonstop mRNA Decay is mostly independent of ZNF-598

Following our evidence of ZNF-598's critical role in No-Go mRNA Decay, we were surprised to observe a minor and NONU-1-independent role for ZNF-598 in Nonstop mRNA Decay (Fig 3H). We suspect NONU-1 is recruited to Nonstop mRNA Decay substrates by an E3 ubiquitin ligase other than ZNF-598. In yeast and mammals, ZNF-598 is known to require at least two collided ribosomes which form a distinct collision interface suitable for ubiquitination (Simms et al., 2017; Juszkiewicz et al., 2018; Matsuo et al., 2020). Given that there are structural differences in collided ribosome conformation during Nonstop mRNA Decay vs. No-Go mRNA Decay (Hilal et al., 2016; Becker et al., 2011), we hypothesize that an E3 ligase other than ZNF-598 is better equipped to recognize ribosomes stalled at the 3'end of an mRNA and trigger Nonstop mRNA Decay. Other E3 ligases have been implicated in surveillance, such as Not4 and RNF10, and

future work will hopefully clarify the recruitment mechanisms of each (Ikeuchi et al., 2019; Garzia and Meyer et al., 2021).

Our Nonstop mRNA Decay reporter does, however, utilize ZNF-598 to some degree. The mild Nonstop mRNA Decay de-repression seen in *znf-598* could be interpreted to indicate that No-Go mRNA Decay-inducing ribosomal collisions are a minority of stalled ribosomes during Nonstop mRNA Decay. We hypothesize that these collisions are worsened in a *nonu-1* mutant and thus recruit ZNF-598 for clearance and decay. These ideas are consistent with other models suggesting multiple types of collisions, with the relative amount of each collision depending on the genetic background (Ikeuchi et al., 2019).

The timing of ribosome rescue and a conserved ubiquitin-binding function for HBS-1

We have previously observed NONU-1 cleavage near the A-site of a collided ribosome (Glover et al., 2020) and we now propose a method for the rescue of this internally-cleaved ribosome (Fig 4G). Structural work positioning *S. cer* Dom34 in a stalled ribosome suggests a requirement for an mRNA-free A-site, as inferred by its beta-loop occluding the mRNA channel (Hilal et al., 2016), and we expect that ribosomes with cleavages in their A-sites would thus be substrates for PELO-1/HBS-1.

However, this model fails to explain how single mutants of *hbs-1* and *pelo-1* have de-repression phenotypes in the *unc-54(rareArg)* reporter (Fig 1H, Fig 4G). Given a model where rescue is downstream of mRNA cleavage, how would deletion of a rescue factor that recognizes cleaved mRNA in a ribosome allow such a terminally-stalled ribosome to complete GFP? We speculate that HBS-1 and PELO-1 may function in an arrest pathway clearing some ribosomes independent of mRNA cleavage and that this pathway occurs on our reporter. PELO-1 could feasibly bind internally-stalled ribosomes independent of cleavage via A-site mRNA displacement as seen by the bacterial rescue factor ArfB (Carbone et al., 2020). An mRNA-cleavage-independent mechanism would thus allow for translation of the downstream GFP on our reporter in *pelo-1* and *hbs-1* mutants. We hypothesize that the leading ribosome in a pileup of collided ribosomes may evade mRNA cleavage and is therefore poised to translate GFP in the absence of rescue.

We also characterized a novel Ub-binding recruitment mechanism for HBS-1. Our functional, computational, and structural results support a model in which HBS-1 function in No-Go mRNA Decay depends on ribosomal ubiquitination (Fig 4). We therefore hypothesize that HBS-1 is

targeted to a stall by its N-terminus after an E3 ligase ubiquitinates sites on the ribosome (*e.g.*, RPS-10 and RPS-20), subsequently localizing PELO-1. Taken together, our findings suggest that HBS-1 and PELO-1 have a route for locating stalled ribosomes via ribosomal ubiquitination and could conceivably utilize this signal during an mRNA-cleavage-independent arrest pathway.

Scenarios leading to missing arginine-stalled ribosomes

Surprisingly, we observed a lack of a notable stalled ribosome peak in either monosomes or disomes at the site on *unc-54(rareArg)*. Instead, we observed a depletion of footprints at the stall (Fig 5, Fig 6). While this result was contrary to the arginine-stalled ribosomal peaks seen in yeast (Meydan et al., 2020; D'Orazio et al., 2019; Zhao et al. 2021), a subdued ribosomal presence at arginine stretches has been previously reported in worms, zebrafish, mice, and humans (Stadler and Fire, 2011; Glover et al., 2020; Han et al., 2020; Arpat et al., 2020). Moreover, our genome-wide analysis at arginine and lysine stretches exhibited a similar depletion (Fig 6D; Fig S8).

This result might be interpreted as faster decoding within arginine and lysine stretches; however, multiple lines of evidence argue against this model:

(1) Ribosomes stalled on our reporter are faced with two of the rarest codons in *C. elegans*. These codons additionally require decoding by very lowly expressed tRNAs. These factors point towards delayed aminoacyl-tRNA accommodation and therefore slow decoding at the stall site.
(2) On our reporter and genome-wide, poly-basic stretches are expected to trigger slower translocation due to interactions between the positively-charged nascent peptide and the peptide exit tunnel (Lu and Deutsch, 2008; Chandrasekaran et al., 2019). We expect these interactions to produce increased ribosomal density within the poly-basic-encoding codons and immediately downstream.
(3) Ribosomes entering a strong stall could conceivably experience faster or discontinuous elongation via a yet-unknown mechanism, akin to "shunting" observed during translation of some viruses (Ryabova and Hohn, 2000). This model would be consistent with lower density at the stall, but would also result in increased density after the stall due to a return to normal elongation. We did not observe an accumulation of ribosomes post-stall on our reporter or genome-wide, thus we do not have support for a faster elongation model. Furthermore, on our reporter, "pushed" ribosomes would have to first produce at least some polyArg peptide to generate the NLS::GFP as observed (Fig 3C).

Given the lack of support for faster elongation through arginines and lysines, we propose several non-mutually exclusive explanations for a missing arginine- and lysine-stalled species:

(1) Ribosomes stalled within the arginine stretch on *unc-54(rareArg)* may experience preferential disassembly by a factor such as the ASC-1 complex (Juszkiewicz et al., 2020). While in agreement with the reduced ribosomal density following the stall on *unc-54(rareArg),* this model is not consistent with the reappearance observed at genome-wide arginines and lysines. Furthermore, it remains unclear why mutations in these factors were not identified in our screens.

(2) Ribosomes decoding strong stall sites may be present as a lowly-abundant, higher-order structure. This structure could consist of trisomes, tetrasomes, pentasomes, etc. which are difficult to visualize and capture via a sucrose gradient. Alternatively, this structure could be a ribosome (monosome or higher-order) with a tightly-bound accessory factor giving rise to a unique footprint size. We considered a broad range of footprint sizes in this work and did not observe this species associated with either monosomes or disomes.

(3) Stalled ribosomes that elicit No-Go mRNA Decay may be unstable in lysates. Ribo-seq is known to preferentially capture elongating ribosomes. If the stalled ribosome species was not easily trapped by translation elongation inhibitors (such as CHX and ANS), the stalled species may escape detection.

(4) No-Go mRNA Decay may occur in a subcellular compartment which is not captured in standard cellular lysis conditions. Given evidence of specialized subcellular compartments for translation and mRNA decay (such as stress granules and P-bodies) (reviewed in Das et al., 2021), some proportion of No-Go mRNA Decay could feasibly occur in a compartment which is lost during lysis.

Despite missing ribosomes at arginine and lysine stretches, we captured a robust signal of ribosomes paused at poly-proline stretches, specifically the Pro-Pro-Gly motif (Fig S8B). This result is consistent with several metazoan disome Ribo-seq studies where proline stalls were most abundant (Han et al., 2020; Arpat et al., 2020). The mechanism of proline stalling is strikingly different from that which is expected during arginine and lysine stalling: peptidyl transfer between proline and glycine proceeds more slowly than at other codons and is aided by eIF5A (Gutierrez et al., 2013; Schmidt et al., 2016; Schuller et al., 2017). Taken together, we conclude that the ribosomal states including PPG-stalled ribosomes are distinct from those states stalled on arginine and lysine stretches.

In light of many recent disome studies, we propose a model where not all stalled ribosomes are captured in standard Ribo-seq preparations, and that existing metazoan disome data represent ribosomes in the PPG-like-stall state. Our work with a validated No-Go mRNA Decay reporter provides evidence that the PPG-like-stall state is distinct from that which occurs during No-Go mRNA Decay. In order to study endogenous targets of No-Go mRNA Decay in metazoans, future work will need to elucidate the unique features of arginine- and lysine-stalled ribosomes to optimize their capture. Identification of this species would therefore provide new molecular insights into decay-inducing ribosomal stalling vs. programmed or transient ribosomal pausing.

ACKNOWLEDGEMENTS

We thank all the members of the Arribere lab for feedback on the manuscript, thoughtful discussion, and technical support. We thank Ben Abrams and the University of California, Santa Cruz (UCSC) Microscopy Facility for assistance with imaging and quantification. This work was supported in part by a T32 Training Grant Fellowship from the National Institute of General Medical Sciences (NIGMS) (5T32GM133391-02) to P.C.M., a National Science Foundation (NSF) Graduate Research Fellowship (NSF DGE-1842400) to M.L.G., an R01 grant from the NIGMS (1R01GM131012-01) to J.A.A., a Searle Scholars award to J.A.A., and start-up funds from UCSC to J.A.A.

AUTHOR CONTRIBUTIONS

P.C.M. and J.A.A conceived the study and designed, conducted, and analyzed experiments. A.L.P. isolated several alleles, performed microscopy and quantification of several strains, and performed the HBS-1 linker and Uba-homology analyses. M.L.G. recovered and mapped Nonstop screen alleles, with some help from T.A.E. with genomic sequencing. N.V. mapped some Nonstop and No-Go screen alleles and performed mutual information analysis. The manuscript was written by P.C.M. and J.A.A, with some sections by A.L.P. and N.V. and input from all authors.

COMPETING INTERESTS

The authors declare no competing interests.

DATA AND MATERIALS AVAILABILITY

The data discussed in this publication have been deposited in NCBI's Gene Expression Omnibus (Edgar et al., 2002) and are accessible through GEO Series accession number GSE187348 (https://www.ncbi.nlm.nih.gov/geo/query/acc.cgi?acc=GSE187348).

SUPPLEMENTARY MATERIALS

Table S1: *C. elegans* strains and oligos

Figures S1-S11

METHODS

C. elegans strain construction and propagation

C. elegans strains were derived from the N2 background (VC2010 [Thompson et al., 2013]), excluding the Hawaiian strain used for suppressor mapping. Animals were grown at 16C or 20C on NGM plates seeded with OP50 as a standard food source (Brenner, 1974). Some strains were obtained from the CGC, which is funded by NIH Office of Research Infrastructure Programs (P40 OD010440).

CRISPR/Cas9 was performed to introduce genomic edits as previously described (Arribere et al., 2014). Multiple independent isolates of each mutation were recovered and observed to have identical phenotypes. Mutant combinations were generated by crossing. A full list of strains, sequences of mutant alleles, and sources is available in Table S1.

Microscopy and image quantification

All worm strains were maintained at 20C. L4 animals were selected and anesthetized in 3uL EN50 with 1mM levamisole in a microscope well slide with a 0.15mm coverslip. A Zeiss AxioZoom microscope was used with a 1.0x objective to acquire all images. The following parameters were used for all images: exposure time 250ms., shift 50%, zoom 80%. 15-25 representative animals were imaged for each strain. All comparisons shown are between images obtained during the same imaging session.

We used FIJI to define the area of the animal, subtract the background, and determine mean pixel intensity for the area of each animal. A mean and standard deviation of fluorescence intensity was calculated for each strain based upon quantification of 15-25 representative images per strain. Student's t-test was used to determine p-values.

EMS mutagenesis and suppressor screens

EMS mutagenesis was performed in three independent screens, one using *unc-54(cc4092)* (nonstop) (Glover et al., 2020) and two using *unc-54(srf1004)* (rareArg), essentially as described (Arribere and Fire, 2018).

Briefly, a large population of each strain was washed with M9 to a final volume of 4mL. EMS was added to a final concentration of ~1mM and animals were incubated at room temperature for 4 hr with nutation. Animals were washed and left overnight at room temperature on NGM plates seeded with OP50. The next day, animals were washed and eggs were collected by hypochlorite treatment. 100-200 eggs were placed on single small NGM+OP50 plates and allowed to propagate. Plates were screened for F2/F3 animals with increased GFP fluorescence and increased movement. Only a single isolate was kept per NGM plate to ensure independence of mutations.

The first rareArg screen was saturated with hits at *znf-598*, occluding our ability to recover additional alleles at other loci. To address this, we constructed a double-balanced strain covering the region of chromosome II harboring *znf-598*, similarly to that done in an NMD suppressor screen (Cali et al., 1999). This strain (WJA 1040) was homozygous on chromosome I for *unc-54(srf1004)* and heterozygous on chromosome II for *mnC1[dpy-10(e128) unc-52(e444) nls190 let-?]* (AG226) and *tra-2(e1095)* (CB2754). Animals homozygous for *mnC1* or homozygous for *tra-2(e1095)* were inviable or Tra/sterile, respectively, allowing us to eliminate recovery of recessive suppressors within the balanced region. This strain was subjected to EMS mutagenesis as described above. Only isolates maintaining the *mnC1/tra-2* heterozygous balancer were kept, as seen by *myo-2::GFP, a* nonTra phenotype, and subsequent viability.

Suppressor mapping and identification

Following recovery of mutants from EMS screens, we employed a Hawaiian SNP mapping approach as described (Doitsidou et al., 2010). We crossed each isolated suppressor to Hawaiian (CB4856) *unc-54(cc4112)* males (expressing an UNC-54::mCherry fusion engineered by CRISPR/Cas9). Cross progeny were isolated and allowed to self-fertilize. The F2 GFP+ progeny were then backcrossed to the *unc-54(cc4112)* males at least 2 times.

After rounds of backcrossing, several phenotypically suppressed animals (~20-30) for a given mutant were pooled together onto a single plate and allowed to starve. Upon starvation, animals were washed off the plate with 1mL EN50, and further washed with EN50 to remove residual *E. coli*. Genomic DNA was extracted after proteinase K treatment and resuspended in 50uL TE pH7.4. 50ng genomic DNA was used as an input for Nextera (Tn5) sequencing library preparation. Libraries were sequenced at the Vincent J. Coates Genomics Sequencing Laboratory at UC Berkeley on a HiSeq 4000 (nonstop) and at Novogene Corporation Inc. UC Davis Sequencing Center on a NovaSeq 6000 (rareArg).

Reads were mapped to the *C. elegans* genome using bowtie2 (version 2.3.4.1). Reads were assigned using GATK (McKenna et al., 2010) and a previously published dataset of Hawaiian SNPs (Thompson et al., 2013). The fraction of reads that were assignable to Hawaiian or N2 animals was calculated across the genome, and linkage was identified by portions of the genome with 0% Hawaiian. Regions of linkage were then manually inspected to identify candidate lesions/loci.

Immunoblotting

Animals were propagated on NGM plates with OP50 until nearly starved, then washed twice with 1ml M9 and flash frozen in liquid nitrogen. Worm pellets were boiled for 10 min at 99C in 1x SDS loading buffer (0.5M Tris-HCl, 100% glycerol, 20% SDS, 1M DTT, 5% bromophenol blue). Samples were vortexed and spun to pellet animals and supernatants were collected. Protein was quantified by Qubit and 15ug protein was run on a 4-20% Mini-PROTEAN(R) TGX Stain-Free Protein gel (Bio-Rad Laboratories, Inc.). Protein was transferred to a low background fluorescence PVDF membrane (Millipore) and the membrane was blocked in 1% nonfat milk in 1x TBST. Anti-HA antibody (Enzo Life Sciences 16B12) was used at a 1:2000 dilution to detect the HA-tagged RPS-10 protein. Secondary antibody staining was performed with 1:15000 LI-COR goat anti-mouse (LI-COR). Imaging was done using a LI-COR Odyssey Imaging System (LI-COR).

RNA-seq

Animals were synchronized by hypochlorite treatment, propagated on NGM plates with OP50 at 16C, and harvested at the L4/young adult stage. Animals were washed off with N50, passed through a 5% sucrose cushion in N50 to remove *E. coli,* and snap frozen in liquid nitrogen. Animals were lysed by grinding in a mortar and pestle cooled in liquid nitrogen in the presence of frozen PLB (20mM Tris pH8.0, 140mM KCl, 1.5mM MgCl2, 1% Triton) and 100ug/mL cycloheximide. Ground animals were stored as frozen powder at -70C.

Total RNA was extracted with trizol, resuspended in TE pH7.4, and quantified by Qubit. Ribosomal RNA was depleted using custom *C. elegans*-specific rRNA hybridization oligos, similar to a planarian protocol as described (Kim et al., 2019). Oligos for this protocol are included in Table S1. Libraries were prepared using an NEBNext Ultra II Directional RNA Library Prep Kit for Illumina sequencing. Libraries were sequenced at Novogene Corporation Inc. UC Davis Sequencing Center on a NovaSeq 6000.

Ribo-seq

For cycloheximide experiments, ground animals as described in RNA-seq were thoroughly mixed with ice cold PLB and 100ug/mL cycloheximide. For anisomycin experiments, animals were ground in frozen PLB and 100ug/mL anisomycin, then mixed with ice cold PLB and 100ug/mL anisomycin. Ribosome::mRNA complexes were obtained via a 10 min clarifying spin at 10,000 rcf at 4C and quantified via Nanodrop A260 measurement. Total OD units were calculated and RNaseI (Ambion) was added as per the following equation: total OD units × 0.3 = ul RNaseI. RNA was digested for 30 min at 23C and immediately loaded onto a chilled 10%-50% sucrose gradient containing 100ug/mL cycloheximide or 100ug/mL anisomycin.

Gradients were spun in an SW41 Ti rotor in an ultracentrifuge at 35,000 rpm for 4.5hrs at 4C. Monosomes and disomes were collected on a fractionator (Brandel) and digested with proteinase K. Monosome and disome RNA was cleaned up by acid phenol chloroform extraction, precipitated, and stored in TE pH7.4. 2ug of purified monosome and disome RNA were run on 15% polyacrylamide gels and size-selected. For cycloheximide experiments, 28-30nt (monosome) and 50-62nt (disome) footprints were excised. For anisomycin experiments, 18-30nt (monosome), 40-49nt (short disome), and 50-62nt (disome) footprints were excised.

Gel-purified RNA was treated with T4 PNK (NEB) to remove 3′phosphates. RNA was then extracted with phenol chloroform, precipitated, and resuspended in TE pH7.4. Pre-adenylated adaptor containing 8nt UMI sequences (JA-AF-34.5) was ligated onto RNA 3′ends with T4 RNA Ligase 2 truncated KQ (NEB). Adaptor-ligated RNA was run on a 15% polyacrylamide gel, and the ligated species was excised, eluted, and precipitated. Reverse transcription was performed using JA-AF-126 and superscript II RT (Thermo Fisher). cDNA was gel-purified and precipitated from a 15% polyacrylamide gel and circularized with CircLigase (Lucigen). Circularized DNA was amplified by PCR (10-14 cycles) using primers containing Illumina-compatible adaptors. Libraries were sequenced at Novogene Corporation Inc. UC Davis Sequencing Center on a NovaSeq 6000.

RNA- and Ribo-seq analyses

RNA- and Ribo-seq reads were trimmed using cutadapt v2.9 (Martin, 2011) and PCR duplicates (identified by the 8nt UMI on AF-JA-34.5) were collapsed using custom scripts. We generated a custom *C. elegans* genome (Ensembl, WBCel235) containing *unc-54(rareArg)* as a separate chromosome and a masked endogenous *unc-54* locus. Reads were mapped to this genome including annotated splice junctions using STAR v2.5.4b (Dobin and Gingeras, 2015 26334920)

allowing for zero mismatches. All downstream analyses were restricted to uniquely mapping reads.

Analyses were performed in python3 and plotted using matplotlib or PyX v0.15 using custom scripts. In rocket plots (*e.g.*, Fig 3F), read counts were median-normalized using DESeq (Anders and Huber, 2010).

Percent readthrough was calculated by finding the average footprints post-rareArg divided by the average footprints pre-rareArg, normalized to the length. This was done omitting 100nts upstream of the 5' end of a ribosome with the first arginine codon in its P-site and 100nts downstream of the 5' end of a ribosome with the last arginine in its P-site. We note that this metric will include effects such as 5' bias into the readthrough calculation; similar calculations with smaller window sizes centered about the stall revealed similar results.

Meta-codon plots of footprint density around a specific motif were created similarly to that done previously (Meydan et al., 2020). Briefly, we generated a list of every occurrence of each amino acid triplet in the *C. elegans* transcriptome. Average normalized monosome and disome density were then plotted by their 3' ends 50nt upstream and downstream of the first nucleotide of the first amino acid in the triplet motif. Dotted lines were drawn at locations indicating the footprint 3' end position when the third codon of each motif is in each ribosomal site.

Ski7 search

To complement a prior (Marshall et al., 2018) search for Ski7 homologs, we carried out a thorough scan of the *C. elegans* genome to identify possible Ski7s. We performed a six-frame translation of the genome and searched for matches to the S3 motif (FXX[P/A]SPD[D/E]) or the N-term of HBS-1/Ski7 (M[A/S]RHR). These efforts failed to identify a protein with an S3 motif, but did identify a single protein with an N-terminal M[A/S]RHR: *h14e04.3*. Further examination of *h14e04.3* revealed a sequence coarsely resembling an S3 motif, but with loss of the central "PD" motif. However, *h14e04.3(Δ)* had no effect on Nonstop mRNA Decay (Fig S2). We note that this approach may have failed to pick up a gene with introns in both the S3 and N-terminal motif, but otherwise should have revealed a Ski7 with a canonical S3 motif, even if unannotated.

HBS-1 linker length calculation

Using the seed alignments from Pfam PF08938 (HBS-1 N-terminus domain) and PF00009 (elongation factor Tu GTP-binding domain), we constructed HMM profiles through hmmbuild.

We used the resulting HMM profiles to search for HBS-1 homologs from genome database files. A custom script identified proteins with hits from both domains, then calculated the distance in between each domain (C-terminus of the N-terminal domain to the N-terminus of the GTP binding domain). Initially, Uniref90 was used as a genome database, but due to the evolutionary interrelatedness of *hbs-1* and *ski-7*, many Ski7 proteins were misidentified as HBS-1. We were able to identify suspected Ski7 proteins with the conserved S3 motif, a hallmark of Ski7 proteins (Marshall et al., 2018). To overcome this issue, we ran the same script against a database of Ensembl human HBS1L orthologs.

Mutual information calculation

Phylogenetic profiling was performed using the PANTHER HMM library Version 16.0 on Ensembl Protists Genome (release 51) combined with MMETSP (Keeling et al., 2014). To identify homologs of proteins from the PANTHER Subfamily HMMs, we used HMMER's hmmsearch function using the following parameters --noali --notextw --cpu 2. We then parsed each output file from HMMER and determined the presence (1) or absence (0) of a homolog in each organism for a sub-family HMM.

Briefly, if multiple subfamily HMMs matched a given protein in a species, the protein was assigned to the subfamily with the highest bit score, and lesser-scoring subfamilies were ignored. Subfamilies with homologs in <5% or >95% of species were discarded; such subfamilies exhibit too little variation for accurate mutual information calculations. Similarly, species with hits for <10% of subfamilies were discarded; such species may represent poor protein assemblies. We also computed the pairwise hamming distance between all species and discarded species until the pairwise hamming distance between all species was at least 0.1, so as to ensure biodiversity. Mutual information for discrete variables was then calculated as: sum(i=0,1); sum(j=0,1) [-log_2(p_ij/(p_i*p_j))]

REFERENCES

Alam, S. L., Sun, J., Payne, M., Welch, B. D., Blake, B. K., Davis, D. R., Meyer, H. H., Emr, S. D., & Sundquist, W. I. (2004). Ubiquitin interactions of NZF zinc fingers. *EMBO Journal, 23*(7), 1411–1421. https://doi.org/10.1038/sj.emboj.7600114. PMID: 15029239

Anders, S., & Huber, W. (2010). Differential expression analysis for sequence count data. Genome biology, 11(10), R106. https://doi.org/10.1186/gb-2010-11-10-r106. PMID: 20979621

Araki, Y., Takahashi, S., Kobayashi, T., Kajiho, H., Hoshino, S. I., & Katada, T. (2001). Ski7p G protein interacts with the exosome and the ski complex for 3′-to-5′ mRNA decay in yeast. *EMBO Journal, 20*(17), 4684–4693. https://doi.org/10.1093/emboj/20.17.4684. PMID: 11532933

Arora, C., Kee, K., Maleki, S., & Keeney, S. (2004). Antiviral protein Ski8 is a direct partner of Spo11 in meiotic DNA break formation, independent of its cytoplasmic role in RNA metabolism. *Molecular Cell, 13*(4), 549–559. https://doi.org/10.1016/s1097-2765(04)00063-2. PMID: 14992724

Arpat, A., Liechti, A., De Matos, M., Dreos, R., Janich, P., & Gatfield, D. (2020). Transcriptome-wide sites of collided ribosomes reveal principles of translational pausing. *Genome Research, 30*(7), 985–999. https://doi.org/10.1101/GR.257741.119. PMID: 32703885

Arribere, J. A., Bell, R. T., Fu, B. X., Artiles, K. L., Hartman, P. S., & Fire, A. Z. (2014). Efficient marker-free recovery of custom genetic modifications with CRISPR/Cas9 in *Caenorhabditis elegans*. *Genetics, 198*(3), 837–846. https://doi.org/10.1534/genetics.114.169730. PMID: 25161212

Arribere, J. A., & Fire, A. Z. (2018). Nonsense mRNA suppression via nonstop decay. *eLife, 7*, 1–23. https://doi.org/10.7554/eLife.33292. PMID: 29309033

Becker, T., Armache, J. P., Jarasch, A., Anger, A. M., Villa, E., Sieber, H., Motaal, B. A., Mielke, T., Berninghausen, O., & Beckmann, R. (2011). Structure of the no-go mRNA decay complex Dom34-Hbs1 bound to a stalled 80S ribosome. *Nature Structural and Molecular Biology, 18(6)*, 715–720. https://doi.org/10.1038/nsmb.2057. PMID: 21623367

Bengtson, M. H., & Joazeiro, C. A. P. (2010). Role of a ribosome-associated E3 ubiquitin ligase in protein quality control. *Nature, 467*(7314), 470–473. https://doi.org/10.1038/nature09371. PMID: 20835226

Brandman, O., Stewart-Ornstein, J., Wong, D., Larson, A., Williams, C. C., Li, G. W., Zhou, S., King, D., Shen, P. S., Weibezahn, J., Dunn, J. G., Rouskin, S., Inada, T., Frost, A., & Weissman, J. S. (2012). A ribosome-bound quality control complex triggers degradation of nascent peptides and signals translation stress. *Cell, 151*(5), 1042–1054. https://doi.org/10.1016/j.cell.2012.10.044. PMID: 23178123

Brenner S. (1974). The genetics of *Caenorhabditis elegans*. *Genetics, 77(*1), 71–94. https://doi.org/10.1093/genetics/77.1.71. PMID: 4366476

Cali, B. M., Kuchma, S. L., Latham, J., & Anderson, P. (1999). *smg-7* is required for mRNA surveillance in *Caenorhabditis elegans*. *Genetics, 151*(2), 605–616. https://doi.org/10.1093/genetics/151.2.605. PMID: 9927455

Carbone, C. E., Demo, G., Madireddy, R., Svidritskiy, E., & Korostelev, A. A. (2020). ArfB can displace mRNA to rescue stalled ribosomes. *Nature Communications, 11*(1). https://doi.org/10.1038/S41467-020-19370-Z. PMID: 33144582

Chandrasekaran, V., Juszkiewicz, S., Choi, J., Puglisi, J. D., Brown, A., Shao, S., Ramakrishnan, V., & Hegde, R. S. (2019). Mechanism of ribosome stalling during translation of a poly(A) tail. *Nature Structural and Molecular Biology, 26*(12), 1132–1140. https://doi.org/10.1038/s41594-019-0331-x. PMID: 31768042

Das, S., Vera, M., Gandin, V., Singer, R. H., & Tutucci, E. (2021). Intracellular mRNA transport and localized translation. *Nature Reviews Molecular Cell Biology, 22*(7), 483–504. https://doi.org/10.1038/s41580-021-00356-8. PMID: 33837370

Davis, Z. H., Mediani, L., Antoniani, F., Vinet, J., Li, S., Alberti, S., Lu, B., Holehouse, A. S., Carra, S., & Brandman, O. (2021). Protein products of nonstop mRNA disrupt nucleolar homeostasis. *Cell Stress & Chaperones, 26*(3), 549–561. https://doi.org/10.1007/s12192-021-01200-w. PMID: 33619693

Dey, G., & Meyer, T. (2015). Phylogenetic Profiling for Probing the Modular Architecture of the Human Genome. *Cell Systems, 1(*2), 106–115. https://doi.org/10.1016/J.CELS.2015.08.006. PMID: 27135799

Dmitriev, S. E., Vladimirov, D. O., & Lashkevich, K. A. (2020). A Quick Guide to Small-Molecule Inhibitors of Eukaryotic Protein Synthesis. *Biochemistry (Moscow), 85*(11), 1389–1421. https://doi.org/10.1134/S0006297920110097. PMID: 33280581

Dobin, A., & Gingeras, T. R. (2015). Mapping RNA-seq Reads with STAR. *Current protocols in bioinformatics, 51*, 11.14.1–11.14.19. https://doi.org/10.1002/0471250953.bi1114s51. PMID: 26334920

Doitsidou, M., Poole, R. J., Sarin, S., Bigelow, H., & Hobert, O. (2010). C. elegans mutant identification with a one-step whole-genome-sequencing and SNP mapping strategy. *PloS one, 5*(11), e15435. https://doi.org/10.1371/journal.pone.0015435. PMID: 21079745

Doma, M. K., & Parker, R. (2006). Endonucleolytic cleavage of eukaryotic mRNAs with stalls in translation elongation. *Nature, 440*(7083), 561–564. https://doi.org/10.1038/nature04530. PMID 16554824

D'Orazio, K. N., Wu, C. C. C., Sinha, N., Loll-Krippleber, R., Brown, G. W., & Green, R. (2019). The endonuclease cue2 cleaves mRNAs at stalled ribosomes during no go decay. *eLife, 8.* https://doi.org/10.7554/eLife.49117.001. PMID: 31219035

Edgar, R., Domrachev, M., & Lash, A. E. (2002). Gene Expression Omnibus: NCBI gene expression and hybridization array data repository. *Nucleic acids research, 30*(1), 207–210. https://doi.org/10.1093/nar/30.1.207. PMID: 11752295

Frischmeyer, P. A., Hoof, A. van, O'Donnell, K., Guerrerio, A. L., Parker, R., & Dietz, H. C. (2002). An mRNA Surveillance Mechanism That Eliminates Transcripts Lacking Termination Codons. *Science, 295*(5563), 2258–2261. https://doi.org/10.1126/SCIENCE.1067338. PMID: 11910109

Garzia, A., Jafarnejad, S. M., Meyer, C., Chapat, C., Gogakos, T., Morozov, P., Amiri, M., Shapiro, M., Molina, H., Tuschl, T., & Sonenberg, N. (2017). The E3 ubiquitin ligase and RNA-binding protein ZNF598 orchestrates ribosome quality control of premature polyadenylated mRNAs. *Nature Communications, 8*. https://doi.org/10.1038/ncomms16056. PMID: 28685749

Garzia, A., Meyer, C., & Tuschl, T. (2021). The E3 ubiquitin ligase RNF10 modifies 40S ribosomal subunits of ribosomes compromised in translation. *Cell Reports, 36(*5), 109468. https://doi.org/10.1016/j.celrep.2021.109468. PMID: 34348161

Glover, M. L., Burroughs, A. M., Monem, P. C., Egelhofer, T. A., Pule, M. N., Aravind, L., & Arribere, J. A. (2020). NONU-1 Encodes a Conserved Endonuclease Required for mRNA Translation Surveillance. *Cell Reports, 30(*13), 4321-4331.e4. https://doi.org/10.1016/j.celrep.2020.03.023. PMID: 32234470

Gutierrez, E., Shin, B. S., Woolstenhulme, C. J., Kim, J. R., Saini, P., Buskirk, A. R., & Dever, T. E. (2013). eIF5A promotes translation of polyproline motifs. *Molecular Cell, 51*(1), 35–45. https://doi.org/10.1016/j.molcel.2013.04.021. PMID: 23727016

Halbach, F., Reichelt, P., Rode, M., & Conti, E. (2013). The yeast ski complex: Crystal structure and RNA channeling to the exosome complex. *Cell, 154*(4), 814–826. https://doi.org/10.1016/j.cell.2013.07.017. PMID: 23953113

Han, P., Shichino, Y., Schneider-Poetsch, T., Mito, M., Hashimoto, S., Udagawa, T., Kohno, K., Yoshida, M., Mishima, Y., Inada, T., & Iwasaki, S. (2020). Genome-wide Survey of Ribosome Collision. *Cell Reports, 31*(5), 107610. https://doi.org/10.1016/j.celrep.2020.107610. PMID: 32375038

Hashimoto, Y., Takahashi, M., Sakota, E., & Nakamura, Y. (2017). Nonstop-mRNA decay machinery is involved in the clearance of mRNA 5′-fragments produced by RNAi and NMD in *Drosophila melanogaster* cells. *Biochemical and Biophysical Research Communications, 484*(1), 1–7. https://doi.org/10.1016/j.bbrc.2017.01.092. PMID:28115162

Hickey, K. L., Dickson, K., Cogan, J. Z., Replogle, J. M., Schoof, M., D'Orazio, K. N., Sinha, N. K., Hussmann, J. A., Jost, M., Frost, A., Green, R., Weissman, J. S., & Kostova, K. K. (2020). GIGYF2 and 4EHP Inhibit Translation Initiation of Defective Messenger RNAs to Assist Ribosome-Associated Quality Control. *Molecular Cell, 79*(6), 950-962.e6. https://doi.org/10.1016/j.molcel.2020.07.007. PMID: 32726578

Hilal, T., Yamamoto, H., Loerke, J., Bürger, J., Mielke, T., & Spahn, C. M. T. (2016). Structural insights into ribosomal rescue by Dom34 and Hbs1 at near-atomic resolution. *Nature Communications, 7*, 1–8. https://doi.org/10.1038/ncomms13521. PMID: 27995908

Hoof, A. van, Staples, R. R., Baker, R. E., & Parker, R. (2000). Function of the Ski4p (Csl4p) and Ski7p Proteins in 3′-to-5′ Degradation of mRNA. *Molecular and Cellular Biology, 20*(21), 8230–8243. https://doi.org/10.1128/MCB.20.21.8230-8243.2000. PMID: 11027292

Hoof, A. van, Frischmeyer, P. A., Dietz, H. C., & Parker, R. (2002). Exosome-Mediated Recognition and Degradation of mRNAs Lacking a Termination Codon. *Science, 295*(5563), 2262–2264. https://doi.org/10.1126/SCIENCE.1067272. PMID: 11910110

Ikeuchi, K., Tesina, P., Matsuo, Y., Sugiyama, T., Cheng, J., Saeki, Y., Tanaka, K., Becker, T., Beckmann, R., & Inada, T. (2019). Collided ribosomes form a unique structural interface to induce Hel2-driven quality control pathways. *The EMBO Journal, 38*(5), 1–21. https://doi.org/10.15252/embj.2018100276. PMID: 30609991

Ishimura, R., Nagy, G., Dotu, I., Zhou, H., Yang, X. L., Schimmel, P., Senju, S., Nishimura, Y., Chuang, J. H., & Ackerman, S. L. (2014). Ribosome stalling induced by mutation of a CNS-specific tRNA causes neurodegeneration. *Science, 345*(6195), 455–459. https://doi.org/10.1126/science.1249749. PMID: 25061210

Juszkiewicz, S., & Hegde, R. S. (2017). Initiation of Quality Control during Poly(A) Translation Requires Site-Specific Ribosome Ubiquitination. *Molecular Cell, 65(*4), 743-750.e4. https://doi.org/10.1016/j.molcel.2016.11.039. PMID: 28065601

Juszkiewicz, S., Chandrasekaran, V., Lin, Z., Kraatz, S., Ramakrishnan, V., & Hegde, R. S. (2018). ZNF598 Is a Quality Control Sensor of Collided Ribosomes. *Molecular Cell, 72*(3), 469-481.e7. https://doi.org/10.1016/j.molcel.2018.08.037. PMID: 30293783

Juszkiewicz, S., Speldewinde, S. H., Wan, L., Svejstrup, J. Q., & Hegde, R. S. (2020). The ASC-1 Complex Disassembles Collided Ribosomes. *Molecular Cell, 79*(4), 603-614.e8. https://doi.org/10.1016/j.molcel.2020.06.006. PMID: 32579943

Kalisiak, K., Kuliński, T. M., Tomecki, R., Cysewski, D., Pietras, Z., Chlebowski, A., Kowalska, K., & Dziembowski, A. (2017). A short splicing isoform of HBS1L links the cytoplasmic

exosome and SKI complexes in humans. *Nucleic Acids Research, 45*(4), 2068–2080. https://doi.org/10.1093/nar/gkw862. PMID 28204585

Keeling, P. J., Burki, F., Wilcox, H. M., Allam, B., Allen, E. E., Amaral-Zettler, L. A., Armbrust, E. V., Archibald, J. M., Bharti, A. K., Bell, C. J., Beszteri, B., Bidle, K. D., Cameron, C. T., Campbell, L., Caron, D. A., Cattolico, R. A., Collier, J. L., Coyne, K., Davy, S. K., Deschamps, P., … Worden, A. Z. (2014). The Marine Microbial Eukaryote Transcriptome Sequencing Project (MMETSP): illuminating the functional diversity of eukaryotic life in the oceans through transcriptome sequencing. *PLoS biology, 12*(6), e1001889. https://doi.org/10.1371/journal.pbio.1001889. PMID: 24959919

Kim, I. V., Ross, E. J., Dietrich, S., Döring, K., Sánchez Alvarado, A., & Kuhn, C. D. (2019). Efficient depletion of ribosomal RNA for RNA sequencing in planarians. *BMC genomics, 20*(1), 909. https://doi.org/10.1186/s12864-019-6292-y. PMID: 31783730

Kostova, K. K., Hickey, K. L., Osuna, B. A., Hussmann, J. A., Frost, A., Weinberg, D. E., & Weissman, J. S. (2017). CAT-tailing as a fail-safe mechanism for efficient degradation of stalled nascent polypeptides. *Science, 357*(6349), 414–417. https://doi.org/10.1126/science.aam7787. PMID: 28751611

Kowalinski, E., Kögel, A., Ebert, J., Reichelt, P., Stegmann, E., Habermann, B., & Conti, E. (2016). Structure of a Cytoplasmic 11-Subunit RNA Exosome Complex. *Molecular Cell, 63*(1), 125–134. https://doi.org/10.1016/j.molcel.2016.05.028. PMID: 27345150

Kulkarni, M., & Smith, H. E. (2008). E1 ubiquitin-activating enzyme UBA-1 plays multiple roles throughout C. elegans development. *PLoS Genetics, 4*(7), 1000131. https://doi.org/10.1371/journal.pgen.1000131. PMID: 18636104

Lareau, L. F., Hite, D. H., Hogan, G. J., & Brown, P. O. (2014). Distinct stages of the translation elongation cycle revealed by sequencing ribosome-protected mRNA fragments. *eLife, 3*, e01257. 1–16. https://doi.org/10.7554/eLife.01257. PMID: 24842990

Lu, J., & Deutsch, C. (2008). Electrostatics in the Ribosomal Tunnel Modulate Chain Elongation Rates. *Journal of Molecular Biology, 384*(1), 73–86. https://doi.org/10.1016/j.jmb.2008.08.089. PMID: 18822297

Lu, J., Wu, T., Zhang, B., Liu, S., Song, W., Qiao, J., & Ruan, H. (2021). Types of nuclear localization signals and mechanisms of protein import into the nucleus. *Cell communication and signaling, 19*(1), 60. https://doi.org/10.1186/s12964-021-00741-y. PMID: 34022911

Marshall, A. N., Han, J., Kim, M., & Van Hoof, A. (2018). Conservation of mRNA quality control factor Ski7 and its diversification through changes in alternative splicing and gene duplication. *Proceedings of the National Academy of Sciences of the United States of*

*America, 115(*29), E6808–E6816. https://doi.org/10.1073/pnas.1801997115. PMID: 29967155

Martin, M. (2011). Cutadapt removes adapter sequences from high-throughput sequencing reads. https://doi.org/10.14806/ej.17.1.200

Matsuo, Y., Tesina, P., Nakajima, S., Mizuno, M., Endo, A., Buschauer, R., Cheng, J., Shounai, O., Ikeuchi, K., Saeki, Y., Becker, T., Beckmann, R., & Inada, T. (2020). RQT complex dissociates ribosomes collided on endogenous RQC substrate SDD1. *Nature Structural and Molecular Biology, 27*(4), 323–332. https://doi.org/10.1038/s41594-020-0393-9. PMID: 32203490

Meydan, S., & Guydosh, N. R. (2020). Disome and Trisome Profiling Reveal Genome-wide Targets of Ribosome Quality Control. *Molecular Cell, 79*(4), 588-602.e6. https://doi.org/10.1016/j.molcel.2020.06.010. PMID: 32615089

McKenna, A., Hanna, M., Banks, E., Sivachenko, A., Cibulskis, K., Kernytsky, A., Garimella, K., Altshuler, D., Gabriel, S., Daly, M., & DePristo, M. A. (2010). The Genome Analysis Toolkit: a MapReduce framework for analyzing next-generation DNA sequencing data. *Genome research, 20*(9), 1297–1303. https://doi.org/10.1101/gr.107524.110. PMID: 20644199

Mi, H., Ebert, D., Muruganujan, A., Mills, C., Albou, L. P., Mushayamaha, T., & Thomas, P. D. (2021). PANTHER version 16: a revised family classification, tree-based classification tool, enhancer regions and extensive API. *Nucleic Acids Research, 49*(D1), D394–D403. https://doi.org/10.1093/nar/gkaa1106. PMID: 33290554

Mueller, T. D., & Feigon, J. (2002). Solution Structures of UBA Domains Reveal a Conserved Hydrophobic Surface for Protein–Protein Interactions. *Journal of Molecular Biology, 319*(5), 1243–1255. https://doi.org/10.1016/S0022-2836(02)00302-9. PMID: 12079361

Navickas, A., Chamois, S., Saint-Fort, R., Henri, J., Torchet, C., & Benard, L. (2020). No-Go Decay mRNA cleavage in the ribosome exit tunnel produces 5′-OH ends phosphorylated by Trl1. *Nature Communications, 11*(1), 1–11. https://doi.org/10.1038/s41467-019-13991-9. PMID: 31913314

Pisareva, V. P., Skabkin, M. A., Hellen, C. U. T., Pestova, T. V., & Pisarev, A. V. (2011). Dissociation by Pelota, Hbs1 and ABCE1 of mammalian vacant 80S ribosomes and stalled elongation complexes. *EMBO Journal, 30*(9), 1804–1817. https://doi.org/10.1038/emboj.2011.93. PMID: 21448132

Prag, G., Misra, S., Jones, E. A., Ghirlando, R., Davies, B. A., Horazdovsky, B. F., & Hurley, J. H. (2003). Mechanism of ubiquitin recognition by the CUE domain of Vps9p. *Cell, 113*(5), 609–620. https://doi.org/10.1016/s0092-8674(03)00364-7. PMID: 12787502

Randles, L., & Walters, K. J. (2012). Ubiquitin and its binding domains. *Frontiers in Bioscience, 17*, 2140–2157. https://doi.org/10.2741/4042. PMID: 22652769

Roach, N. P., Sadowski, N., Alessi, A. F., Timp, W., Taylor, J., & Kim, J. K. (2020). The full-length transcriptome of *C. elegans* using direct RNA sequencing. *Genome research, 30*(2), 299–312. https://doi.org/10.1101/gr.251314.119 PMID: 32024661

Ryabova, L. A., & Hohn, T. (2000). Ribosome shunting in the cauliflower mosaic virus 35S RNA leader is a special case of reinitiation of translation functioning in plant and animal systems. *Genes & development, 14*(7), 817–829. PMID: 10766738

Saito, S., Hosoda, N., & Hoshino, S. I. (2013). The Hbs1-Dom34 protein complex functions in non-stop mRNA decay in mammalian cells. *Journal of Biological Chemistry, 288*(24), 17832–17843. https://doi.org/10.1074/jbc.M112.448977. PMID: 23667253

Schmidt, C., Becker, T., Heuer, A., Braunger, K., Shanmuganathan, V., Pech, M., Berninghausen, O., Wilson, D. N., & Beckmann, R. (2016). Structure of the hypusinylated eukaryotic translation factor eIF-5A bound to the ribosome. *Nucleic Acids Research, 44*(4), 1944–1951. https://doi.org/10.1093/nar/gkv1517. PMID: 26715760

Schuller, A. P., Wu, C. C., Dever, T. E., Buskirk, A. R., & Green, R. (2017). eIF5A Functions Globally in Translation Elongation and Termination. *Molecular Cell, 66*(2), 194–205.e5. https://doi.org/10.1016/j.molcel.2017.03.003. PMID: 28392174

Shao, S., & Hegde, R. S. (2014). Reconstitution of a Minimal Ribosome-Associated Ubiquitination Pathway with Purified Factors. *Molecular Cell, 55*(6), 880–890. https://doi.org/10.1016/j.molcel.2014.07.006. PMID: 25132172

Shoemaker, C. J., Eyler, D. E., & Green, R. (2010). Dom34:Hbs1 Promotes Subunit Dissociation and Peptidyl-tRNA Drop-Off to Initiate No-Go Decay. *Science, 330*(6002), 369–372. https://doi.org/10.1126/SCIENCE.1192430. PMID: 20947765

Shoemaker, C. J., & Green, R. (2011). Kinetic analysis reveals the ordered coupling of translation termination and ribosome recycling in yeast. *Proceedings of the National Academy of Sciences of the United States of America, 108*(51). https://doi.org/10.1073/pnas.1113956108. PMID: 22143755

Simms, C. L., Yan, L. L., & Zaher, H. S. (2017). Ribosome Collision Is Critical for Quality Control during No-Go Decay. *Molecular Cell, 68*(2), 361-373.e5. https://doi.org/10.1016/j.molcel.2017.08.019. PMID: 28943311

Simms, C. L., Yan, L. L., Qiu, J. K., & Zaher, H. S. (2019). Ribosome Collisions Result in +1 Frameshifting in the Absence of No-Go Decay. *Cell Reports, 28*(7), 1679-1689.e4. https://doi.org/10.1016/j.celrep.2019.07.046. PMID: 31412239

Stadler, M., & Fire, A. Z. (2011). Wobble base-pairing slows in vivo translation elongation in metazoans. *RNA, 17*(12), 2063–2073. https://doi.org/10.1261/RNA.02890211. PMID: 22045228

Sundaramoorthy, E., Leonard, M., Mak, R., Liao, J., Fulzele, A., & Bennett, E. J. (2017). ZNF598 and RACK1 Regulate Mammalian Ribosome-Associated Quality Control Function by Mediating Regulatory 40S Ribosomal Ubiquitylation. *Molecular Cell, 65*(4), 751-760.e4. https://doi.org/10.1016/j.molcel.2016.12.026. PMID: 28132843

Thompson, O., Edgley, M., Strasbourger, P., Flibotte, S., Ewing, B., Adair, R., Au, V., Chaudhry, I., Fernando, L., Hutter, H., Kieffer, A., Lau, J., Lee, N., Miller, A., Raymant, G., Shen, B., Shendure, J., Taylor, J., Turner, E. H., Hillier, L. W., … Waterston, R. H. (2013). The million mutation project: a new approach to genetics in *Caenorhabditis elegans*. *Genome research, 23*(10), 1749–1762. https://doi.org/10.1101/gr.157651.113. PMID: 23800452

Wang, J., Zhou, J., Yang, Q., & Grayhack, E. J. (2018). Multi-protein bridging factor 1(Mbf1), Rps3 and Asc1 prevent stalled ribosomes from frameshifting. *eLife, 7*, 1–26. https://doi.org/10.7554/eLife.39637. PMID: 30465652

Zhao, T., Chen, Y.-M., Li, Y., Wang, J., Chen, S., Gao, N., & Qian, W. (2021). Disome-seq reveals widespread ribosome collisions that promote cotranslational protein folding. *Genome Biology, 22*(1), 1–35. https://doi.org/10.1186/S13059-020-02256-0. PMID: 33402206

Zinoviev, A., Ayupov, R. K., Abaeva, I. S., Hellen, C. U. T., & Pestova, T. V. (2020). Extraction of mRNA from Stalled Ribosomes by the Ski Complex. *Molecular Cell, 77*(6), 1340-1349.e6. https://doi.org/10.1016/j.molcel.2020.01.011. PMID: 32006463